Fermi National Accelerator Laboratory

FERMILAB-Pub-94/218-E

E665

Nuclear Shadowing, Diffractive Scattering and Low Momentum Protons in μXe Interactions at 490 GeV

The E665 Collaboration

Fermi National Accelerator Laboratory
P.O. Box 500, Batavia, Illinois 60510

July 1994

Submitted to *Zeitschrift* für P*hysik C.*

Operated by Universities Research Association Inc. under Contract No. DE-AC02-76CHO3000 with the United States Department of Energy

Disclaimer

Nuclear shadowing, diffractive scattering and low momentum protons in μXe interactions at 490 GeV

THE E665 COLLABORATION

Submitted to Zeitschrift für Physik C

revised August 1994

Abstract

The production of charged hadrons is studied in μXe and μD interactions at 490 GeV beam energy. The data were taken at the Tevatron at Fermilab with the E665 spectrometer, equipped with a streamer chamber as vertex detector. Differences between the μXe and μD data are explained by cascading of hadrons in the Xe nucleus. The average multiplicity of charged hadrons in μXe scattering is compared to previously published pXe scattering data and is found to be strongly reduced. This is traced back to the low number of 'projectile' collisions in μXe interactions. From a study of the x_{Bj} dependence of hadron production in μXe scattering, and by considering events with a large rapidity gap, evidence is found for a significant contribution of diffractive scattering, which is enhanced in the kinematic region where shadowing of the cross section is observed. This result supports recent models in which diffractive scattering and nuclear shadowing are closely related.

M. R. Adams [6], M. Aderholz [11], S. Aïd [9,a], P. L. Anthony [10,b], M. D. Baker [10], J. Bartlett [4], A. A. Bhatti [13,c], H. M. Braun [14], W. Busza [10], T.J. Carroll [11], J. M. Conrad [5], G. Coutrakon [4,d], R. Davisson [13], I. Derado [11], S. K. Dhawan [15], W. Dougherty [13], T. Dreyer [1], K. Dziunikowska [8], V. Eckardt [11], U. Ecker [14,a], M. Erdmann [1,e], A. Eskreys [7], J. Figiel [7], H. J. Gebauer [11], D. F. Geesaman [2], R. Gilman [2,f], M. C. Green [2,g], J. Haas [1], C. Halliwell [6], J. Hanlon [4], D. Hantke [11], V. W. Hughes [15], H. E. Jackson [2], D. E. Jaffe [6,h], G. Jancso [11], D. M. Jansen [13,i], K. Kadija [11], S. Kaufman [2], R. D. Kennedy [3], T. Kirk [4,j], H. G. E. Kobrak [3], S. Krzywdzinski [4], S. Kunori [9], J. J. Lord [13], H. J. Lubatti [13], D. McLeod [6], S. Magill [6,j], P. Malecki [7], A. Manz [11], H. Melanson [4], D. G. Michael [5,k], W. Mohr [1], H. E. Montgomery [4], J. G. Morfin [4], R. B. Nickerson [5,l], S. O'Day [9,m], K. Olkiewicz [7], L. Osborne [10], V. Papavassiliou [15,j], B. Pawlik [7], F. M. Pipkin [5,*], E. J. Ramberg [9,m], A. Röser [14,o], J. J. Ryan [10], C. W. Salgado [4], A. Salvarani [3,p], H. Schellman [12], M. Schmitt [5,q], N. Schmitz [11], K. P. Schüler [15,r], H. J. Seyerlein [11], A. Skuja [9], G. A. Snow [9], S. Söldner-Rembold [11,s], P. H. Steinberg [9,*], H. E. Stier [1,*], P. Stopa [7], R. A. Swanson [3], R. Talaga [9,j], S. Tentindo-Repond [2,t], H.-J. Trost [2,u], H. Venkataramania [15], M. Wilhelm [1], J. Wilkes [13], Richard Wilson [5], W. Wittek [11], S. A. Wolbers [4], T. Zhao [13]

(E665 Collaboration)

[1] *Albert-Ludwigs-Universität Freiburg i. Br., Germany*
[2] *Argonne National Laboratory, Argonne, IL USA*
[3] *University of California, San Diego, CA USA*
[4] *Fermi National Accelerator Laboratory, Batavia, IL USA*
[5] *Harvard University, Cambridge, MA USA*
[6] *University of Illinois, Chicago, IL USA*
[7] *Institute for Nuclear Physics, Krakow, Poland*
[8] *Institute for Nuclear Physics, Academy of Mining and Metallurgy, Krakow, Poland*
[9] *University of Maryland, College Park, MD USA*
[10] *Massachusetts Institute of Technology, Cambridge, MA USA*
[11] *Max-Planck-Institut für Physik, Munich, Germany*
[12] *Northwestern University, Evanston, IL USA*
[13] *University of Washington, Seattle, WA USA*
[14] *University of Wuppertal, Wuppertal, Germany*
[15] *Yale University, New Haven, CT USA*

Present addresses:
[a] Alaskaweg 20, 22145 Hamburg, Germany.
[b] Lawrence Livermore National Laboratory, Livermore CA 94550, USA.
[c] The Rockefeller University, New York NY 10021, USA.
[d] Loma Linda University Medical Center, Loma Linda CA 92350, USA.
[e] DESY, Notkestrasse 85, 22603 Hamburg, Germany.
[f] Rutgers University, Piscataway, NJ 08855, USA.
[g] LeCroy Research Systems, Spring Valley, NY 10977, USA.
[h] Laboratoire de l'Accèlèrateur Linèaire, F-91405 Orsay, France.
[i] Los Alamos National Laboratory, Los Alamos, NM 87545, USA.
[j] Argonne National Laboratory, Argonne, IL 60439, USA.
[k] California Institute of Technology, Pasadena, CA 91125, USA.
[l] Oxford University, Oxford OX1 3RH, UK.
[m] Fermi National Accelerator Laboratory, Batavia, IL 60510, USA.
[o] Universität Bochum, 44801 Bochum, Germany.
[p] A.T. & T., Bell Labs, 2000 North Naperville Road, Naperville, IL USA.
[q] University of Wisconsin, Madison, WI 53706, USA.
[r] Superconducting Super Collider Laboratory, Dallas, TX 75237, USA.
[s] Albert-Ludwigs-Universität Freiburg, 79104 Freiburg, Germany.
[t] Northern Illinois University, Dekalb, IL 60115, USA.
[u] Texas A&M University, College Station,

* Deceased

1 Introduction

In many models of interactions of particles with nuclei the interaction is interpreted as a sequence of independent collisions of the incident particle (henceforth denoted as the projectile) or its constituents with single nucleons inside the nucleus (multiple scattering) [1]. In addition, the products of each projectile collision may interact with other nucleons of the nucleus and produce more particles. This process is called intra-nuclear cascading [2, 3].

In various respects lepton-induced reactions differ fundamentally from hadron-induced ones. To a good approximation the lepton-induced reactions proceed via the exchange of a single virtual photon (γ^*). For not too low values of the Bjorken-scaling variable x_{Bj} (non-shadowing region) the virtual photon is expected to interact with only one nucleon of the target nucleus [4–6]. The only mechanism for particle multiplication in this case is intra-nuclear cascading, which therefore can be investigated in a direct and clean way. This is in contrast to the hadron-induced reactions, where multiple collisions of the projectile constitute another important mechanism for particle production.

Insight into the mechanism of hadron-production on nuclei may be gained by measuring hadron multiplicities as a function of the number of projectile or cascade interactions. Several methods were proposed to estimate, for a given nucleus, the average number of projectile or cascade interactions. One measure is given by the number of knock-out protons [7–9], with velocities β between ≈ 0.3 and ≈ 0.7, corresponding to laboratory momenta between 300 and 900 MeV/c. Such protons may either originate directly from the projectile collisions or they may have been knocked out in the cascade process [10, 11]. They are to be distinguished from the protons with $\beta \lesssim 0.3$ which mainly result from the evaporation of the final nucleus [11]. Using a streamer chamber, protons with $0.3 < \beta < 0.7$ are observed as 'grey tracks', where the streamer density is significantly higher than that of a minimum ionizing particle.

Analyses using grey tracks have been restricted so far mainly to experiments with incident hadrons [7–21] with the exception of [3], where the interaction of 150 GeV muons in nuclear emulsion was studied.

The x_{Bj} range considered in the present analysis is $0.002 < x_{Bj} < 0.30$. It covers not only the kinematic region where no shadowing is observed in the cross section per nucleon ($x_{Bj} > 0.02$) but also the region of significant shadowing ($x_{Bj} < 0.02$) [22, 23]. It would be interesting to know whether the variation of the shadowing effect with x_{Bj} is accompanied by a variation of hadron production with x_{Bj}.

Related to this is the question of how the relative contributions from diffractive scattering to the cross section and to hadron production depend on x_{Bj}. In the theory of lepton-nucleus interactions there is a close relation between nuclear shadowing and diffractive scattering [24, 25, 5, 26–34] (see also Sect. 2). This has implications on the x_{Bj} dependence of hadron production which have not yet been tested experimentally.

The x_{Bj} dependence of hadron production in lepton-nucleus scattering has so far been addressed in [3, 35] and in another analysis from this experiment [36].

In the present analysis hadron production in μXe interactions is studied as a function of the number of grey tracks and compared with hadron production in μD scattering. The results are also compared with those from a pp, pXe experiment [14, 17, 37, 38]. In addition, in μXe and μD scattering the x_{Bj} dependence of hadron production and effects of diffraction are investigated in detail.

The layout of the paper is as follows. In Sect. 2 the theoretical expectations concerning the relation between nuclear shadowing and diffractive scattering are compiled. Sect. 3 deals with the experimental details. The experimental results are presented in Sect. 4 and a summary is given in Sect. 5.

2 Nuclear shadowing and diffractive scattering in lepton-nucleus interactions

The relation between nuclear shadowing and diffractive scattering in lepton-nucleus interactions has been discussed in various papers [24, 25, 5, 26–34]. The basic ideas and predictions are compiled in the following Section, in order to prepare the discussion of the results from the present analysis in Sect. 4.

Nuclear shadowing in charged-lepton nucleus scattering implies that (at fixed x_{Bj} and Q^2) the total cross section $\sigma(\gamma^* A)$ on a nucleus (with mass number A) is less than A times the total cross section $\sigma(\gamma^* N)$ on a nucleon

$$\sigma(\gamma^* A) = A \cdot \sigma(\gamma^* N) - \Delta\sigma \,. \tag{1}$$

Since via the optical theorem the total cross section is related to the imaginary part of the amplitude T_{el} for elastic $\gamma^* A$ scattering, the behaviour of $\sigma(\gamma^* A)$ may be discussed in terms of T_{el}. T_{el} can be written as

$$T_{el} = \sum_{i=1}^{A} T_i \,, \tag{2}$$

where i denotes the number of nucleons involved in the interaction. The diagrams corresponding to the two lowest terms in (2) are sketched in Fig. 1. It is the single scattering term T_1 (Fig. 1a), which yields a contribution to $\sigma(\gamma^* A)$ proportional to A (first term on the right hand side of (1)). The shadowing term $\Delta\sigma$ is determined by T_i ($i \geq 2$), where the double-scattering term T_2 (Fig. 1b) provides the dominant contribution.

The double scattering term T_2 receives contributions from all possible intermediate states X (Fig. 1b). At high energies the dominant contribution to T_2 is given by those states X for which the amplitude $F(\gamma^* N \rightarrow XN)$ is predominantly imaginary. This is the case for diffractively produced systems X.

There is an interesting difference between hadron-nucleus and lepton-nucleus (or photon-nucleus) scattering. While in the former elastic scattering (on a single nucleon) yields the dominant contribution to T_2 and thus to nuclear shadowing, this contribution is negligibly small in the latter, due to the low $\gamma^* N$ elastic cross section.

Apart from possible changes of the nucleon structure in the nuclear medium, the only source of nuclear shadowing in lepton-nucleus scattering is coming from reinteractions of diffractively produced states excited by the virtual photon [30].

Thus the presence of nuclear shadowing in lepton-nucleus scattering (at certain x_{Bj} and Q^2) requires the presence of diffractive production (at the same x_{Bj} and Q^2). To be more precise, it requires the presence of coherent diffractive production (CD), with a similar x_{Bj} dependence as that of nuclear shadowing. There may be in addition incoherent diffractive production (ID).

Some numerical predictions obtained within the model of [31, 32] are given in [39]. The interesting observations for low x_{Bj}, where nuclear shadowing occurs, are:

- the ratio of the coherent diffractive to the total inelastic cross section increases with increasing A and is in μXe scattering a factor of ~ 6 higher than in μD scattering and a factor of ~ 2 higher than in μp scattering
- the ratio of the incoherent diffractive to the total inelastic cross section decreases with increasing A and is a factor of ~ 4 lower in μXe than in μD scattering
- the ratio of coherent diffractive to incoherent diffractive cross section is $\sim 1/2$ in μD and $\sim 10/1$ in μXe scattering.

In addition it is found that the ratio of the total diffractive cross section to the shadowing term $\Delta\sigma$ depends only weakly on x_{Bj}, and that the incoherent diffractive cross section persists even at large x_{Bj}, where coherent diffractive production and nuclear shadowing are low.

3 Experimental details

3.1 Measurement of muons, charged hadrons and of electromagnetic energy

The data were taken with the E665 detector, which is described in [40]. It consists of a vertex spectrometer and a forward spectrometer. The main component of the vertex spectrometer is a photographic streamer chamber, which is located inside a 15 kG vertex magnet and which surrounds the target. The streamer chamber provides momentum measurement ($\Delta p/p \approx 0.02\, p/(\mathrm{GeV/c})$) for nearly all charged hadrons with a momentum between 0.2 GeV/c and 10 GeV/c. The main components of the forward spectrometer are another magnet, a set of multiwire proportional and drift chambers, an electromagnetic calorimeter and a muon identifier behind a hadron absorber. In the forward spectrometer the momenta of charged hadrons and muons in the momentum range 10 GeV/c $< p <$ 500 GeV/c are measured with a relative error of $\Delta p/p \approx 5 \times 10^{-5}\, p/(\mathrm{GeV/c})$.

In the present analysis only charged hadrons with a momentum greater than 200 MeV/c are considered, because particles at lower momentum are often absorbed in the target. No corrections are applied for this cut. This means that all results to be presented refer to hadrons with $p \geq 200$ MeV/c.

A muon is identified by matching the track segment in the muon identifier (downstream of the hadron absorber) with the particle trajectory reconstructed in the detectors upstream of the absorber.

Charged particles, which are not identified as muons, are treated as hadrons. Positive hadrons that are classified as "grey tracks" (see below) or for which the quantity $x_F(m_\pi)$ is less than -0.20 ($x_F(m_\pi)$ is the Feynman-x (see Sect. 3.3) for a particle assuming a pion mass) are assigned the proton mass. All remaining hadrons are treated as pions. This procedure is suggested by a Monte Carlo calculation which shows that in μD scattering, with $E_\mu = 490$ GeV and $W > 8$ GeV, about 50% of the positive hadrons with $x_F(m_\pi) < -0.20$ are protons. In μXe scattering the fraction of protons in this kinematic range is expected to be considerably higher.

Further details of the experiment, in particular concerning the processing of the streamer chamber data, may be found in [41, 42].

3.2 Grey tracks

The classification of a positive hadron as a "grey track" is done on the basis of the streamer density of the particle track in the streamer chamber picture. In this paper, a particle is called a "grey track", if it has a momentum between 200 and 600 MeV/c, and if the streamer density as observed in the streamer chamber picture is clearly higher than that of a minimum ionizing particle. It should be noted that this definition of a grey track is different from the one used in [14], where a momentum interval 100–600 MeV/c is considered. However, in the comparisons of data from this experiment with those from [14], to be presented in this paper, a momentum window from 200 to 600 MeV/c is chosen for both data sets.

Grey tracks were counted in the μD and μXe data and independently in two laboratories. The results of the two laboratories agreed within 11%, compared to a statistical error of 2.5 %. The grey tracks are assumed to be predominantly protons. Contaminations from pions and kaons are expected from particle trajectories forming a small angle relative to the optical axis, thus yielding tracks with enhanced streamer densities in the streamer chamber picture. From their angular distributions in the laboratory frame the contamination of the sample of grey tracks by pions and kaons is estimated as $\sim 40\%$ and $(15 \pm 9)\%$ for the μD and μXe data respectively. The efficiency for identifying a proton in the momentum region 200 to 600 MeV/c is estimated by comparing the measured average number of protons (remaining after the subtraction of the contamination) in the momentum window in μD scattering with the corresponding number expected in the Lund Monte Carlo model. The resulting efficiency is $\varepsilon_{\mu\mathrm{D}} = \varepsilon_{\mu\mathrm{Xe}} = (75 \pm 15)\%$. This number includes the acceptance of the detector for positive particles in the backward hemisphere, which is 96% on the average. The efficiency $\varepsilon_{\mathrm{pXe}}$ in the pXe data is estimated to be higher by about 10% as compared to $\varepsilon_{\mu\mathrm{Xe}}$ in μXe scattering: $\varepsilon_{\mathrm{pXe}} = \varepsilon_{\mu\mathrm{Xe}} \cdot [1 + (0.1 \pm 0.1)]$.

It should be noted that in μD scattering only a small fraction of all protons fall into the momentum window from 200 to 600 MeV/c. According to the Lund Monte Carlo model (LEPTO 4.3, JETSET 4.3 [43, 44]) there are on the average 0.60 protons per event, of which 12% (i.e. 0.07 protons per event) have momenta between 200 and 600 MeV/c. For comparison, the average multiplicity of positive (negative) hadrons in this momentum window amounts to 0.40 (0.39).

Because of the large contamination of the grey tracks sample in μD scattering by pions and kaons no quantitative results are given on grey tracks in the μD sample.

Since the low momentum protons were not simulated consistently in the Monte Carlo calculations for the various reactions, the data presented in this paper are uncorrected data. As far as ratios of average multiplicities of particles are concerned the corrections for losses and contaminations will largely cancel. Since in this analysis basically correlations of the number of grey tracks (n_g) with other variables are of interest, the precise value of n_g being irrelevant, corrections to the data are considered unimportant. In some cases (see Sect. 4.7), where grey tracks are not involved, the data were also corrected for the experimental inefficiencies, using correction factors determined by Monte Carlo calculations (correction method B as described in [42]). The qualitative features of the corrected data were found to be identical with those of the uncorrected ones and the conclusions drawn from the measured data were confirmed.

The errors of the measured quantities, quoted in the tables and drawn in the figures are purely statistical.

3.3 Definition of kinematic variables and selection of the data

The deep-inelastic muon-nucleon scattering process can be described by the exchange of a single virtual photon. In the following the target nucleon is assumed to be at rest in the laboratory frame, which means that the internal momenta of the nucleons within the nucleus are ignored. The kinematic variables of the event are then defined by

$$Q^2 = -2m_\mu^2 + 2E_\mu E'_\mu - 2p_\mu p'_\mu \cos\Theta$$ negative square of the virtual photon four-momentum,

$$W^2 = -Q^2 + 2M\nu + M^2$$ squared invariant mass of the hadronic system,

$$x_{Bj} = \frac{Q^2}{2M\nu}$$ Bjorken-x,

$$\nu = E_\mu - E'_\mu$$ leptonic energy transfer in the laboratory frame,

where m_μ is the muon mass, E_μ (E'_μ) is the laboratory energy and p_μ (p'_μ) the laboratory momentum of the incident (outgoing) muon, Θ is the muon scattering angle in the laboratory frame and M is the nucleon mass.

The hadron variables used are Feynman-x, $x_F = 2p_L^*/W$, and the cms rapidity

$$y^* = \frac{1}{2} \ln \frac{E_h^* + p_L^*}{E_h^* - p_L^*}.$$

E_h and p_L are the energy and the longitudinal momentum (relative to the direction of the virtual photon) of the hadron in the laboratory frame. The hadronic center-of-mass frame (cms) is defined by the system formed by the virtual photon and the target nucleon, and the variables in this frame are labelled by a $*$. The forward and backward hemispheres correspond to the regions x_F (or y^*) > 0 and x_F (or y^*) < 0, respectively.

The definition of the final data sample, to be used in the analysis, is similar to the one given in [42]. In particular the kinematic quantities are restricted to the regions

$$\begin{aligned} Q^2 &> 1\ \mathrm{GeV}^2 \\ 8 &< W < 30\ \mathrm{GeV} \\ x_{Bj} &> 0.002 \\ 50 &< \nu < 400\ \mathrm{GeV}. \end{aligned} \tag{3}$$

In contrast to [42] events which are consistent with exclusive production of ρ^0 or ϕ mesons are included in the data sample. The upper limit in ν is applied in order to exclude the kinematic region in which radiative effects are large. Residual contamination by events with a high-energy bremsstrahlung photon in the final state is removed by applying, for both the Xe and D data set, additional cuts on the energy deposited in the electromagnetic calorimeter [42]: an event is removed

- if the number of energy clusters in the calorimeter is ≤ 2 or, alternatively, if the highest-energy cluster contains more than 80% of the total energy deposited in the calorimeter
- and if, in addition, the total energy deposited in the calorimeter is $\geq 0.5\ \nu$.

After all cuts, the total number of events is 6071 for μD and 1999 for μXe scattering. The average values of ν, W, Q^2 and x_{Bj} for the μXe sample are 172.1 GeV, 17.0 GeV, 10.0 GeV^2 and 0.044; those of the μD sample are very close.

The data from this experiment will be compared with those from the NA5 experiment [14, 17, 37, 38] on pp and pXe reactions at a beam momentum of 200 GeV/c. The comparison is favored by the fact that important features of the two experiments are similar: a streamer chamber was used as vertex detector in both experiments and the identification of grey tracks was performed in the same way as in E665; the cms energy of the proton–nucleon system is 19.42 GeV, which is comparable to the average W of the E665 data. The NA5 data samples, which include only events with at least three hadrons in the final state, consist of 3340 pp and 1730 pXe events.

3.4 Monte Carlo predictions

The data will be compared with predictions of the VENUS Monte Carlo model, which describes hadron production in reactions on nuclei by the interaction of strings in nuclear matter [45–47]. QCD effects and diffractive processes are not included in the model. The program version used in the present analysis is VENUS 4.10.

For the comparison of Monte Carlo predictions with (uncorrected) experimental data the identification efficiency and the acceptance of particles (see Sects. 3.1, 3.2) were simulated in the Monte Carlo calculations. The relevant numbers are compiled in Table 1.

Two important parameters of the VENUS model are r_B and r_M. Two strings or a string and a nucleon will interact as soon as their distance in space-time is below r_B (if a baryon is formed) or below r_M (if a meson is formed). By varying the parameters r_B and r_M the model was tuned to approximately reproduce the measured values of the quantities $\langle Q_T\rangle_{\mu\mathrm{Xe}}$, $\langle Q_T\rangle_{\mu\mathrm{D}}$, $\langle n_g\rangle_{\mu\mathrm{Xe}}$ and $\langle n_B\rangle_{\mu\mathrm{Xe}} - \langle n_B\rangle_{\mu\mathrm{D}}$. These quantities, which will be defined and discussed in Sect. 4, are compared with the VENUS prediction as a function of ν in Fig. 2. The resulting values of r_B and r_M are 0.50 fm and 0.40 fm respectively, which are close to those used in [42] ($r_B = 0.55$ fm, $r_M = 0.35$ fm) and also to the default values ($r_B = 0.65$ fm, $r_M = 0.35$ fm).

4 Results

4.1 Average number of projectile collisions

A useful quantity in the discussion of nuclear effects is the effective number of nucleons in the nucleus, A_{eff}, defined by

$$\frac{A_{\mathrm{eff}}}{A} = \frac{\sigma_{hA}}{A \cdot \sigma_{hN}}, \tag{4}$$

where A is the target mass number, σ_{hN} is the inelastic cross section in hadron-nucleon collisions and σ_{hA} is the absorption cross section in hadron-nucleus collisions [48–50]. In the framework of the Glauber model the inverse of (4) is interpreted as the average number of projectile collisions with nucleons in the hadron-nucleus interaction,

$$\langle \nu_{\mathrm{proj}} \rangle = \frac{A \cdot \sigma_{hN}}{\sigma_{hA}}. \tag{5}$$

$\langle \nu_{\mathrm{proj}} \rangle$ in (5) actually measures the average number of inelastic hadron-nucleon collisions, assuming that the hadron-nucleon cross section is independent of the number of collisions experienced. According to (5) $\langle \nu_{\mathrm{proj}} \rangle$ is directly related to the strength of the shadowing effect. In the absence of shadowing $\langle \nu_{\mathrm{proj}} \rangle$ is equal to 1.

For pXe interactions (5) yields a value of [51, 52]

$$\langle \nu_{\mathrm{proj}} \rangle_{\mathrm{pXe}} = \frac{131.29 \times (31.8 \pm 0.4)\mathrm{mb}}{(1290 \pm 50)\mathrm{mb}} = 3.24 \pm 0.13\ . \tag{6}$$

Although lepton-nucleon (nucleus) scattering differs from hadron-nucleon (nucleus) scattering in many respects, formula (5) may also be applied to lepton scattering, when the incident hadron h is replaced by the virtual photon (γ^*). In particular at small values of x_{Bj} ($\lesssim 0.02$), where the fluctuation length for the $\gamma^* \to q\bar{q}$ transition is large as compared to the size of the nucleon (nucleus), the virtual photon exhibits features similar to those of hadrons [5, 24–34, 53–55]. Using the measurements of the shadowing effect in μXe scattering from [22, 23] one obtains

$$
\begin{array}{llll}
\langle \nu_{\rm proj} \rangle_{\mu \rm Xe} & = 1.19 \pm 0.05 & \text{for } x_{Bj} < 0.02 & \text{(shadowing region)} \\
 & \approx 1.0 & \text{for } x_{Bj} > 0.02 & \text{(non-shadowing region)} \\
 & & & \\
 & = 1.09 \pm 0.04 & \text{average over E665 data} & \\
 & & \text{used in this analysis}, & \qquad (7)
\end{array}
$$

where the quoted errors are statistical. The systematic errors are of the order of 0.13. Equations (6) and (7) suggest a significantly smaller number of projectile collisions in μXe than in pXe scattering. This is also confirmed by the analysis in [42]: in contrast to pXe and pp scattering, the average multiplicity of charged hadrons in μXe scattering is not significantly enhanced in the central rapidity region relative to μD scattering, from which it was concluded that the average number of projectile collisions in μXe scattering, in the kinematic range (3), is close to 1.

4.2 Dependence on the leptonic energy transfer ν

In Fig. 2 three quantities, which are sensitive to nuclear effects, are plotted as a function of ν: the average total hadronic net charge $\langle Q_T \rangle$, the average number of grey tracks $\langle n_g \rangle$ and the difference of average charged backward multiplicities $\langle n_B \rangle_{\mu \rm Xe} - \langle n_B \rangle_{\mu \rm D}$ in μXe and μD scattering. If $\langle \nu_{\rm proj} \rangle$ is close to 1, $\langle n_B \rangle_{\mu \rm Xe} - \langle n_B \rangle_{\mu \rm D}$ is, to a good approximation, the multiplicity of charged hadrons from cascading. The average hadronic net charge $\langle Q \rangle$ is defined as the difference $\langle n^+ \rangle - \langle n^- \rangle$ of the average multiplicities of positive and negative hadrons, where n^+ includes the grey tracks. $\langle Q_T \rangle$ is the average hadronic net charge, integrated over the whole rapidity region. In all three quantities, apart from $\langle Q_T \rangle$ in μD scattering, there is a slight tendency for a decrease with increasing ν. However, the ν dependence is so weak that it is justified to combine the data from all ν for the subsequent discussion.

4.3 Grey tracks as an efficient means for tagging events with cascade interactions in μXe scattering

In Figs. 3 and 4 μXe events with grey tracks ($n_g \neq 0$) are compared with those without grey tracks ($n_g = 0$) and with μD data. The average hadronic net charge $\mathrm{d}\langle Q \rangle / \mathrm{d}y^*$ is plotted as a function of y^* in Fig. 3. Within the experimental errors no differences are seen in the forward region between the three data samples. In the backward region the (μXe, $n_g = 0$) data points are close to, although slightly above, the μD data points, while the (μXe, $n_g \neq 0$) sample exhibits a huge bump, due to hadrons from cascading in the Xe nucleus. This demonstrates that grey tracks can be used very efficiently to separate those events in which cascade interactions occur. The cascade interactions give rise to an enhanced production of mainly positive particles in the backward hemisphere [42].

In Fig. 4 the ratio of average charged multiplicities $R = \langle n \rangle_{\mu\mathrm{Xe}} / \langle n \rangle_{\mu\mathrm{D}}$ in μXe and μD scattering is displayed as a function of y^*. The multiplicity n includes the grey tracks. The copious production of additional positive and negative hadrons in μXe scattering at negative y^* is clearly seen in the $n_g \neq 0$ subsample. Some positive hadrons from cascading are also present in the $n_g = 0$ sample, although reduced by an order of magnitude relative to the $n_g \neq 0$ sample. From Fig. 4 it can be seen that some cascade hadrons are also produced in the central region, at low $|y^*|$.

4.4 Multiplicity of grey tracks

In Fig. 5 the multiplicity distribution of grey tracks ($P(n_g)$) for μXe scattering from this experiment is compared with that for pXe scattering. The fraction of events with n_g grey tracks decreases approximately exponentially with increasing n_g, with a much steeper slope for the μXe than for the pXe data. The average number of grey tracks $\langle n_g \rangle$ is 0.56 ± 0.02 and 2.53 ± 0.08 in μXe and pXe scattering respectively (Table 2).

Using (6) and (7) the average number of grey tracks per projectile interaction is determined as

$$s_{\mathrm{proj}} = \frac{\langle n_g \rangle}{\langle \nu_{\mathrm{proj}} \rangle} = \begin{cases} 0.51 \pm 0.03 & \text{in } \mu\mathrm{Xe} \\ 0.78 \pm 0.04 & \text{in pXe scattering}. \end{cases} \tag{8}$$

$\langle n_g \rangle_{\mu\mathrm{Xe}}$ is considerably (by a factor of 4.5) lower than $\langle n_g \rangle_{\mathrm{pXe}}$, as expected from the lower number of projectile interactions in μXe scattering. On the other hand, the numbers in (8) show that $\langle n_g \rangle$ is not proportional to $\langle \nu_{\mathrm{proj}} \rangle$ and seems to rise faster than linearly with $\langle \nu_{\mathrm{proj}} \rangle$. This observation remains valid even when the different identification efficiencies (and its systematic error) for protons in pXe and μXe scattering are taken into account. A stronger than linear dependence of $\langle n_g \rangle$ on $\langle \nu_{\mathrm{proj}} \rangle$ was also suggested by the experimental data on hadron nucleus reactions [56, 7, 8, 57]. Those data were consistent with an $A^{2/3}$ behavior of $\langle n_g \rangle$ [9–11], which is to be compared with the $A^{1/3}$ behavior of $\langle \nu_{\mathrm{proj}} \rangle$.

Another interesting aspect in such comparisons is the contribution of diffractive processes. As diffractive scattering gives rise to less grey tracks on the average than non-diffractive scattering (see Sect. 4.8) the strength of the contribution from diffraction will be reflected in the value of $\langle n_g \rangle$. The contribution of diffractive processes in μXe interactions is discussed in Sects. 4.8 and 4.9.

4.5 Average hadronic net charge

Whenever a proton is struck, either in the projectile collision or in the cascade process, the total hadronic charge Q_T of the secondary particles increases by 1. Since the fraction of protons in a nucleus is Z/A, and assuming identical cross sections for interactions with protons and neutrons, one obtains the following relation between $\langle Q_T \rangle$

and the total number ν_c of collisions with nucleons in the nucleus [58, 59, 2]:

$$\langle Q_T \rangle = \frac{Z}{A} \langle \nu_c \rangle + \text{charge of projectile} \; . \tag{9}$$

The charge of the projectile is 1 for pXe and 0 (virtual photon) for μXe scattering. The average numbers of collisions $\langle \nu_c \rangle$, as derived from the experimental values of $\langle Q_T \rangle$ using (9), are listed in Table 2. As in the case of $\langle n_g \rangle$, $\langle \nu_c \rangle_{\mu \mathrm{Xe}}$ is much smaller than $\langle \nu_c \rangle_{\mathrm{pXe}}$. The average number of collisions with nucleons per projectile interaction, $\langle \nu_c \rangle / \langle \nu_{\mathrm{proj}} \rangle$, is roughly equal in μXe and pXe scattering (Table 2), implying an approximate equal number of cascade interactions per projectile collision in both reactions. The last column in Table 2 contains ratios of quantities measured in pXe and μXe scattering. One can see that for all quantities considered, namely $\langle n_g \rangle$, $\langle \nu_c \rangle$, $\langle n_B \rangle_{\mathrm{Xe}} - \langle n_B \rangle_{\mathrm{D}}$ and $\langle Q_T \rangle_{\mathrm{Xe}} - \langle Q_T \rangle_{\mathrm{D}}$, the ratio is of the order of the ratio $\langle \nu_{\mathrm{proj}} \rangle_{\mathrm{pXe}} / \langle \nu_{\mathrm{proj}} \rangle_{\mu \mathrm{Xe}}$ of the average number of projectile collisions.

In Fig. 6 the average hadronic net charge is plotted as a function of n_g for the total rapidity range and for the backward and forward regions separately. The data for both μXe and pXe scattering exhibit a strong correlation between $\langle Q_T \rangle$ and n_g. This is expected since n_g is supposed to rise with ν_c, as does $\langle Q_T \rangle$. As can be seen from Figs. 6b and c, the correlation is restricted to the backward region.

According to (9) $\langle Q_T \rangle$ is directly related to $\langle \nu_c \rangle$. However, due to the momentum cut at 200 MeV/c and to the finite acceptance for charged particles (see Table 1) there are large fluctuations in the measured Q_T, which makes Q_T less suitable for an estimate of $\langle \nu_c \rangle$ on an event-by-event basis than n_g.

With $\nu_c = 1$ (only one projectile interaction and no cascade interactions), $\langle Q_T \rangle$ in (9) acquires its minimum possible value: $\langle Q_T \rangle^{\min} = (\frac{Z}{A} + \text{charge of projectile}) = 0.41$ and 1.41 for μXe and pXe scattering respectively. In the limit $n_g \to 0$ the measured value of $\langle Q_T \rangle$ is slightly larger than $\langle Q_T \rangle^{\min}$ (Fig. 6a). This is to be expected since for the $n_g = 0$ sample $\langle \nu_c \rangle$ is greater than 1, because not every collision produces a proton in the momentum window 200-600 MeV/c, and not every proton in this momentum window is accepted and identified as a grey track. The difference $\langle Q_T \rangle_{\mathrm{pXe}} - \langle Q_T \rangle_{\mu \mathrm{Xe}}$ at $n_g = 0$ is close to 1, as expected from the charge of the proton projectile (9).

From Fig. 6c it can be seen that the charge of the projectile manifests itself nearly exclusively in the forward hemisphere. In fact, the average hadronic forward charge is roughly compatible with the charge of the projectile, so that according to (9) the average hadronic backward charge is directly proportional to $\langle \nu_c \rangle$ (Fig. 6b).

Fits of straight lines ($a_Q + b_Q \cdot n_g$) to the data points of $\langle Q_T \rangle$ in Fig. 6a yield the parameter values listed in Table 3. With the fitted values of a_Q and b_Q and using (9) one obtains the relations

$$\langle \nu_c(n_g) \rangle_{\mu \mathrm{Xe}} = (2.08 \pm 0.13) + (3.72 \pm 0.14) \cdot n_g \tag{10}$$

$$\langle \nu_c(n_g) \rangle_{\mathrm{pXe}} = (2.07 \pm 0.15) + (4.17 \pm 0.10) \cdot n_g \, . \tag{11}$$

From (10) and (11) it follows that by fixing n_g one selects subsamples of μXe and pXe events which have similar $\langle \nu_c \rangle$, with slightly larger $\langle \nu_c \rangle$ for pXe. Note that this does not imply equal values of $s_c = \langle n_g \rangle / \langle \nu_c \rangle$ in μXe and pXe scattering.

4.6 Average hadronic multiplicity

For the comparison of the hadronic multiplicity in μXe and pXe interactions, the average charged multiplicity for the interaction on the nucleus is divided by the average charged multiplicity for the respective elementary reaction on deuterium:

$$R(n_g)_{\mu\mathrm{Xe}} = \frac{\langle n(n_g)\rangle_{\mu\mathrm{Xe}}}{\langle n\rangle_{\mu\mathrm{D}}} \quad \text{or} \quad R(n_g)_{\mathrm{pXe}} = \frac{\langle n(n_g)\rangle_{\mathrm{pXe}}}{\langle n\rangle_{\mathrm{pD}}}. \tag{12}$$

In this way trivial differences between the muon and the proton reaction are reduced. Also energy dependences are removed, as has been shown in [16]. In (12) n_g denotes the number of grey tracks in the reaction on Xe, and the average multiplicities $\langle n\rangle_{\mu\mathrm{D}}$ and $\langle n\rangle_{\mathrm{pD}}$ enter as scale factors, independent of n_g. In the expression (12) for R the multiplicities $n(n_g)_{\mu\mathrm{Xe}}$ and $n(n_g)_{\mathrm{pXe}}$ include the grey tracks. The ratio obtained by excluding the grey tracks will be denoted by $\overline{R}$.

As no data are available from the NA5 experiment on pD scattering, the multiplicities in pD scattering are constructed from the data on pp scattering by assuming [14, 42]

$$\left.\begin{array}{l} n^+(\mathrm{pD}){=}n^+(\mathrm{pp}) \\ n^-(\mathrm{pD}){=}n^-(\mathrm{pp}) \end{array}\right\} \text{ in the forward region and}$$

$$\left.\begin{array}{l} n^+(\mathrm{pD}){=}0.5*(n^+(\mathrm{pp})+n^-(\mathrm{pp})) \\ n^-(\mathrm{pD}){=}0.5*(n^+(\mathrm{pp})+n^-(\mathrm{pp})) \end{array}\right\} \text{ in the backward region.}$$

By this procedure the ratios R and $\overline{R}$ are increased for positive particles and reduced for negative particles, in the backward hemisphere.

$\overline{R}(n_g)$ is plotted as a function of n_g in Fig. 7a for μXe and pXe scattering. The curves represent the function

$$\overline{R}(n_g) = \frac{1}{2}\left[1 + \langle\nu_{\mathrm{proj}}(n_g)\rangle\right] \tag{13}$$

where $\langle\nu_{\mathrm{proj}}(n_g)\rangle$ denotes the average number of projectile interactions for a fixed number of grey tracks. For pXe $\langle\nu_{\mathrm{proj}}(n_g)\rangle$ was calculated in the framework of the model described in [8], assuming the probability distribution $\pi_{\mathrm{pXe}}(\nu_{\mathrm{proj}})$ for ν_{proj} projectile interactions to be given by the Glauber model [60, 61] and using the measured value $[\langle n_g\rangle/\langle\nu_{\mathrm{proj}}\rangle]_{\mathrm{pXe}} = 0.78$. For μXe scattering $\pi_{\mu\mathrm{Xe}}(\nu_{\mathrm{proj}})$ was obtained by the model of [31], and the prescription of [8] was applied using the measured value $[\langle n_g\rangle/\langle\nu_{\mathrm{proj}}\rangle]_{\mu\mathrm{Xe}} = 0.51$. The resulting dependences $\langle\nu_{\mathrm{proj}}(n_g)\rangle$ are displayed in Fig. 7b. The important point to note is that there is a strong variation of $\langle\nu_{\mathrm{proj}}(n_g)\rangle$ only in the pXe reaction and that in the μXe reaction $\langle\nu_{\mathrm{proj}}(n_g)\rangle$ is very low, even at large values of n_g.

The form (13) is obtained in a number of models [62–70]. A simple interpretation of (13) is given as follows: in a projectile-nucleon collision the projectile and the target each contribute equally to the produced multiplicity. In a projectile-nucleus collision there are ν_{proj} projectile collisions, each giving the same contribution to the average multiplicity, from which relation (13) follows if shadowing in deuterium is neglected ($\langle\nu_{\mathrm{proj}}\rangle = 1$). The data from previous hadron-nucleus experiments [71, 7, 10, 17–19] were found to be fairly well described by (13) and this is confirmed by the pp, pXe data from the NA5 experiment [17] (Fig. 7a). This is not the case for the μXe data which at high n_g lie above the prediction. In order to understand this behaviour one should keep in mind that formula (13) comprises the effects from the projectile and cascade interactions. While in pXe scattering both contribute about equally, in μXe scattering the excess multiplicity comes nearly entirely from the cascade process. Thus in μXe scattering the variation of $\overline{R}(n_g)$ with n_g reflects the dependence on $\langle\nu_c\rangle$ rather than on $\langle\nu_{\text{proj}}\rangle$.

$R(n_g)$, which includes the grey tracks, is plotted for positive, negative and all charged particles in Fig. 8, and for the backward and forward region in Fig. 9. Straight line fits to the data points for positive, negative and all charged particles in Fig. 8 yield the slope values listed in Table 4. The patterns of the data points for $R(n_g)$ in the backward and forward region resemble those for $\langle Q\rangle$ in Fig. 6: a strong correlation with n_g in the backward region and practically no correlation in the forward region. In the backward region $R(n_g)$ seems to depend essentially on n_g, and thus on $\langle\nu_c\rangle$, as does $\langle Q\rangle$.

For the subsequent discussion three rapidity regions (see Table 5) are chosen, in which different mechanisms of hadron production are supposed to dominate: a target fragmentation region (target), a central region (central) and a projectile fragmentation region (projectile). Note that gaps have been left between the regions to reduce transition effects.

Fig. 10 displays $R(n_g)$ as a function of n_g for the three rapidity intervals defined in Table 5, for all charged hadrons and for positive and negative hadrons separately. In nearly all plots of Fig. 10, $R(n_g)$ is clearly correlated with n_g and in the limit $n_g \to 0$ $R(n_g)$ tends to values close to or slightly above 1. The latter behaviour is expected, as with the requirement $n_g = 0$ μXe events are selected in which $\langle\nu_c\rangle$ is small (see (10) and (11)), and which therefore resemble very much the events on D.

Consider first the target fragmentation region (Figs. 10a,b,c). This region, which is dominated by particles from cascading, exhibits a strong increase of $R(n_g)$ with n_g. The increase is stronger for positive than for negative particles, however it is similar for μXe and pXe scattering. The latter fact implies that the number of particles from the cascade process is essentially a function of $\langle\nu_c\rangle$, see (10) and (11). In another hadron-nucleus analysis [20], where the ratio of average multiplicities of shower particles (all particles except those identified as protons from ionization) was considered, this ratio was found to be a function of the number of projectile collisions $\langle\nu_{\text{proj}}(n_g)\rangle$. The difference as compared to the results presented here is attributed to the inclusion or exclusion of grey tracks in the multiplicity ratio.

In the central rapidity region (Figs. 10d,e,f) direct production of particles by projectile collisions is expected to dominate. This is indeed confirmed by the data: in the pXe reaction the average number of projectile collisions $\langle\nu_{\text{proj}}(n_g)\rangle$ increases with increasing n_g, resulting in a larger multiplicity of produced (positive and negative) hadrons. The very weak increase of $R(n_g)$ in μXe scattering, where $\langle\nu_{\text{proj}}(n_g)\rangle$ varies only weakly with n_g, indicates a small contribution of hadrons from cascading.

In the projectile fragmentation region (Figs. 10g,h,i) $R(n_g)$ decreases with increasing n_g, similarly for positive and negative particles, and similarly in the μXe and pXe reaction, with a slope $\Delta R(n_g)/\Delta n_g$ of ~ -0.07. With increasing n_g the average number of (projectile and/or cascade) collisions rises. The more collisions occur, the more the available energy is distributed among more particles, leading to a depletion of the high-rapidity region [72–74, 16].

The similarity in Figs. 10g,h,i between μXe and pXe scattering would imply that the depletion of fast hadrons is essentially a function of $\langle \nu_c(n_g) \rangle$, rather than of $\langle \nu_{\mathrm{proj}}(n_g) \rangle$. This is in contrast to the analysis of hadron-nucleus scattering data in [20], where the depletion was consistent with a dependence on $\langle \nu_{\mathrm{proj}}(n_g) \rangle$. The data in Figs. 10g,h,i thus indicate that the μXe data, as compared to the pXe data, exhibit a stronger depletion of fast hadrons than expected on the basis of the number of projectile collisions.

It should be noted that in μXe scattering the bulk of the data is at low n_g (see Fig. 5) and that the depletion of forward hadrons is only seen in the very small sample of events with large n_g. For this reason one was not able to see the depletion in analyses which integrated over all n_g [42, 36].

Predictions from the VENUS model are compared with the data in Figs. 2, 5, 6, 8 and 9. The model describes the gross qualitative features of the data: the strong decrease of $P(n_g)$ with increasing n_g, the strong correlation of $\langle Q_B \rangle$ and $R(n_g)$ with n_g, and the trend of the differences between μXe and pXe scattering. The model does not reproduce the tail of $P(n_g)$ at high n_g (Fig. 5), and it is not able to describe quantitatively $R(n_g)$ and the differences between $R(n_g)_{\mu\mathrm{Xe}}$ and $R(n_g)_{\mathrm{pXe}}$ (Figs. 8 and 9).

4.7 Comparison of hadron production in the shadowing and non-shadowing regions of μXe scattering

The μXe data sample is subdivided into a sample where significant shadowing of the per-nucleon cross section is observed [22, 23] and a sample in which shadowing may be neglected :

- shadowing region A : $x_{Bj} < 0.02$ (denoted by 'sha' in the figures)
- non-shadowing region B: $x_{Bj} > 0.02$ (denoted by 'nsh' in the figures)

A comparison of hadron production in the two samples is of great interest as it may give insight into the mechanism of shadowing. Shadowing is usually associated with the hadronlike behaviour of photons as contrasted to the pointlike behaviour in the non-shadowing region. The ranges of x_{Bj}, Q^2, ν and W covered by samples A and B and the respective average values of kinematic quantities are listed in Table 6. As can be seen, the two samples differ significantly from each other in all four variables, the shadowing region being characterized by low x_{Bj} and Q^2 and high ν and W.

The gross qualitative features of hadron production are found to be similar in the samples A and B. As examples Figs. 11 to 15 show $P(n_g)$ versus $n_g, \langle Q \rangle$ versus $n_g, R(n_g)$ versus n_g, $\mathrm{d}\langle Q \rangle/\mathrm{d}y^*$ versus y^* and $\mathrm{d}(\langle n \rangle_{\mu\mathrm{Xe}} - \langle n \rangle_{\mu\mathrm{D}})/\mathrm{d}y^*$ versus y^* for the two data sets. The bumps in the distributions for the shadowing and non-shadowing region in Figs. 14b, 15a and 15b appear to be shifted relative to each other. This shift is due to the different average W in the two regions. One can conclude that cascading of hadrons, which is the dominant nuclear effect in the hadronic system, is similar in the shadowing and non-shadowing region.

In order to investigate possible differences in hadron production between the shadowing and non-shadowing region in more detail, the average values of those quantities which are most sensitive to nuclear effects in the hadronic system, $\langle Q_T \rangle$, $\langle n_g \rangle$ and $\langle n_B \rangle_{\mu \mathrm{Xe}} - \langle n_B \rangle_{\mu \mathrm{D}}$, are listed for the samples A and B in Table 7 and are plotted as a function of x_{Bj} in Fig. 16. The three quantities $\langle Q_T \rangle$, $\langle n_g \rangle$ and $\langle n_B \rangle_{\mu \mathrm{Xe}} - \langle n_B \rangle_{\mu \mathrm{D}}$ are, of course, strongly correlated, as the grey tracks contribute to each of them. Except for $\langle Q_T \rangle_{\mu \mathrm{D}}$, there is a clear trend, in all three quantities, of enhanced particle production with increasing x_{Bj}, implying more nuclear effects in the non-shadowing than in the shadowing region of μXe scattering. The same trend is also seen in Figs. 11, 14 and 15 : In the non-shadowing region, as compared to the shadowing region, the fraction of events with a grey track is enhanced (Fig. 11), and the average hadronic charge (Fig. 14b) and the difference of average multiplicities between μXe and μD scattering (Figs. 15a and b) are in general higher.

It is known that radiative effects are very different in the low-x_{Bj} and high-x_{Bj} region. Those effects have been addressed by the event selections described in Sect. 3.3. However, in order to make sure that the observed differences between the shadowing and non-shadowing region are not due to residual radiative effects, the comparisons were repeated using tighter cuts in ν and/or in the energy deposited in the calorimeter. No significant change of the results was observed, and in particular the trend of the data with x_{Bj} remained the same. The smearing $\Delta = (x_{Bj,\mathrm{true}} - x_{Bj,\mathrm{apparent}})/x_{Bj,\mathrm{true}}$ in the variable x_{Bj} due to the presence of radiative events in the final data samples was estimated by Monte Carlo studies, using the program GAMRAD [75], which is based on the work of [76]. The mean and rms of Δ were found to be of the order of 0.002 and 0.013 respectively, similarly in the μD and μXe data samples. Smearing effects in x_{Bj} due to residual radiative events are thus negligible.

Since in the present data sample the variables ν and x_{Bj} are strongly correlated (see Table 6, regions A and B), one may ask whether the observed trend with x_{Bj} is due to a ν dependence. For this reason the samples A and B were further cut (giving samples A′ and B′) such that the resulting average values of ν agreed (see Table 6). Samples A′ and B′ still differ significantly in the average Q^2. This redefinition of shadowing and non-shadowing regions has practically no effect on the experimental results, as can be seen from Table 7.

The differences between the samples A and B (or A′ and B′) in μXe scattering can therefore not be attributed to a ν dependence. The same conclusion can be drawn from Fig. 17, in which $\langle Q_T \rangle$, $\langle n_g \rangle$ and $\langle n_B \rangle_{\mu \mathrm{Xe}} - \langle n_B \rangle_{\mu \mathrm{D}}$ are plotted as a function of ν for samples A and B separately: In both samples there is no evidence for a ν dependence.

Because of the strong correlation between Q^2 and x_{Bj} in the present data sample (Table 6) and because of limited statistics it was not possible to disentangle the dependences on Q^2 and x_{Bj}. With the restriction to samples A or B respectively, the three quantities $\langle Q_T \rangle_{\mu \mathrm{Xe}}$, $\langle n_g \rangle_{\mu \mathrm{Xe}}$ and $\langle n_B \rangle_{\mu \mathrm{Xe}} - \langle n_B \rangle_{\mu \mathrm{D}}$ still exhibit an increase with increasing Q^2 (Fig. 18).

In contrast to μXe scattering $\langle Q_T \rangle$ does not depend on x_{Bj} in μD scattering (Fig. 16 and Table 7). As has been shown in [42], after correction $\langle Q_T \rangle_{\mu \mathrm{D}}$ is consistent with the value 0.50, which is expected from charge conservation when nuclear effects are negligible.

Another interesting observation is made from Figs. 12 and 13: Hadron production seems to be identical in samples A and B of μXe scattering as soon as n_g (and thus also $\langle \nu_c \rangle$) is fixed. The differences found above are therefore to be attributed to the difference in the multiplicity distribution $P(n_g)$ of grey tracks between samples A and B, as seen in Fig. 11 mainly at $n_g = 0$ and $n_g = 1$. This means that the relative statistical weight of the data points at different n_g in Figs. 12 and 13 is different for samples A and B.

The enhanced hadron production in the non-shadowing region is in contradiction to [77, 5, 28], where a multiplicity decrease by 20 - 40% is predicted when passing (at fixed ν) from the shadowing to the non-shadowing region. It is argued that at high x_{Bj} the virtual photon is absorbed uniformly over the whole volume of the nucleus ('volume effect'), whereas at low x_{Bj}, where shadowing is observed, the interaction occurs mainly in the front part of the nucleus ('surface effect'). Consequently, the mean distance within the nucleus available for cascading is lower in the former than in the latter case, suggesting a reduced hadron production in the non-shadowing region. Possible explanations for the experimental observations which are opposite to this expectation are discussed in the next Section.

The VENUS model gives a reasonable qualitative description of the data in Figs. 11, 12, 13. The x_{Bj} dependence observed for μXe scattering in Fig. 16 is not reproduced by the model, in which diffractive processes are not included.

4.8 Contribution from large-rapidity-gap events

It has been suggested [24, 25, 5, 26–34] that a significant contribution to the cross section in the shadowing region comes from diffractive scattering. As explained in Sect. 2, the appearance of shadowing is actually directly related to the presence of diffractive scattering. A study of the contribution from diffractive scattering may therefore help to understand the differences in hadron production observed in the previous Section between the shadowing and the non-shadowing region.

By diffractive scattering one usually understands a process which proceeds via the exchange of an object with vacuum quantum numbers, called a pomeron. In deep-inelastic lepton-*nucleon* scattering, diffractive events consist of a quasi-elastically scattered target nucleon (which may or may not dissociate into several hadrons), well separated in rapidity from the rest of the hadronic system (diffractive system) resulting from the dissociation of the projectile (exchanged vector boson or the colorless state into which it fluctuates). This is in contrast to ordinary deep-inelastic scattering, where due to the color exchange between the struck quark and the nucleon remnant the whole rapidity region is populated with final state hadrons. The event topology for diffractive events in lepton-*nucleus* scattering is expected to be similar to that in lepton-*nucleon* scattering, because cascade effects in the nucleus are strongly suppressed for these events [29, 78, 79]. Furthermore, in the coherent diffractive production the target nucleus remains in the ground state, so that there is a vanishing hadronic activity and no cascading in the nucleus fragmentation region. Notice, that [39] predicts a dominance of the coherent diffractive production over the incoherent diffractive production in interactions on heavy nuclei (see Sect. 2). Experimentally little or no cascading will be reflected in low values of $\langle Q_T \rangle$, $\langle n_g \rangle$ and $\langle n_B \rangle_{\mu \mathrm{Xe}} - \langle n_B \rangle_{\mu \mathrm{D}}$.

As an attempt to define subsamples of events in which diffractive scattering (with dissociation of the projectile) is enhanced or suppressed, the events are classified as to whether they contain a large rapidity gap or not. The rapidity gap (Δy^*) is defined as the width of the rapidity region between the rapidity of the target nucleon (before it is struck) and the lowest rapidity of a charged hadron in the event. In this procedure grey tracks are not considered, that is to say that the large-rapidity-gap events are allowed to have grey tracks within the rapidity gap. This takes account of the fact that part of the low momentum protons produced in diffractive events are observed as grey tracks. In the present analysis no distinction is made between coherent and incoherent diffractive scattering. Since the average momentum of the Xe nucleus in a coherent event is of the order 70 MeV/c these events will produce no grey tracks (due to the momentum cut at 200 MeV/c).

Diffractive events in which the nucleon dissociates contain several low-momentum hadrons. With the above definition of the rapidity gap and because of the momentum cut at 200 MeV/c only a subsample of these events will be contained in the large-rapidity-gap event samples.

The fraction of events (F) with a rapidity gap greater than Δy^* is plotted as a function of Δy^* in Fig. 19. At low Δy^* ($\Delta y^* \lesssim 2.0$) the fraction is higher for μD than for μXe scattering, as expected from the higher backward multiplicities in μXe. Only at very large Δy^* ($\Delta y^* \gtrsim 3.5$), where the fraction is of the order of a few percent, does the μXe fraction exceed the μD fraction. This is a first indication of diffractive scattering, which is expected to be relatively stronger in μXe than in μD scattering (see Sect. 2).

This interpretation is supported by Fig. 20, in which F is plotted for the shadowing and non-shadowing region separately. In the samples where diffractive events are expected to dominate ($\Delta y^* \gtrsim 3.5$) the fraction of large-rapidity-gap events is significantly bigger in the shadowing than in the non-shadowing region. The effect is more pronounced in μXe scattering. All this is consistent with the concept that nuclear shadowing is intimately connected with diffractive scattering and that in the shadowing region the relative contribution of diffractive events increases with the atomic mass A (see Sect. 2).

In the following, events with a rapidity gap greater than 2 are called large-rapidity-gap (LRG) events. The gap cut at 2 is suggested by studies of diffractive scattering in hadron-nucleon scattering [80]. It should be emphasized that with this rather generous definiton of LRG events the LRG event sample will contain a considerable amount of non-diffractive events. The complementary event sample, called SRG (small-rapidity-gap) event sample in the following, will be rather free of diffractive events. This is also supported by Fig. 20, if the difference in F between the shadowing and non-shadowing region is attributed to diffractive scattering. Large-rapidity-gap events are also being studied at HERA [81–83], although at larger values of Q^2 ($Q^2 \lesssim 100$ GeV^2) and W ($W \lesssim 300$ GeV). Due to the large rapidity region available in those experiments the minimum gap width can be much larger than in the present experiment, yielding LRG event samples, which contain only a small fraction of non-diffractive events.

In Fig. 21 the fraction of LRG events is plotted as a function of x_{Bj}. While the μD fractions are nearly independent of x_{Bj}, the μXe data exhibit a significant drop with increasing x_{Bj}. The experimental data for μD scattering and their comparison to the VENUS prediction suggest that with a rapidity gap size ≥ 2 the LRG samples in both regions A and B contain a considerable amount of non-diffractive events. At large x_{Bj}, the presence of cascade hadrons pushes the fraction of LRG events in μXe scattering to lower values. This effect is supported by the VENUS predictions at large x_{Bj} for μD and μXe scattering, drawn as dashed and solid lines in Fig. 21. With decreasing x_{Bj} this effect seems to diminish and to be compensated by the presence of diffractive events. Neither the fractions in the shadowing region ($x_{Bj} < 0.02$) nor those in the non-shadowing region ($x_{Bj} > 0.02$) show a clear dependence on ν or Q^2 (not shown).

In μXe scattering not only is the fraction of LRG events different in the shadowing and non-shadowing region (Figs. 20 and 21) but the properties of the LRG events seem to exhibit some dependence on x_{Bj} (Fig. 22), namely a decrease of $\langle Q_T \rangle$, $\langle n_g \rangle$ and $\langle n_B \rangle_{\mu\mathrm{Xe}} - \langle n_B \rangle_{\mu\mathrm{D}}$ with decreasing x_{Bj}. One interpretation of these observations is that in the shadowing region (as compared to the non-shadowing region) the LRG event sample is more enriched with diffractive events and the fraction of diffractive events is larger. This is in nice agreement with the predicted dominance of coherent diffractive production in the shadowing region of μXe scattering [39].

From a comparison of the μXe data points in Fig. 16 with the SRG data points in Fig. 22 one can conclude that the x_{Bj} dependence seen in Fig. 16 is due to diffractive scattering. An estimate [39] of the suppression of $\langle Q_T \rangle$ and $\langle n_g \rangle$ at low x_{Bj}, based on a calculation of the fraction of diffractive events as a function of x_{Bj}, is indeed in good agreement with the μXe data in Fig. 16.

It is interesting to note that even after removal of the LRG events, and thus of practically all diffractive events, the expectation of an enhanced hadron production at low x_{Bj}, based on the distance in the nucleus available for cascading (see Sect. 4.7), is not confirmed (SRG data points in Fig. 22).

In the literature several other effects are discussed which are relevant for hadron production on a nucleus [84–87]: the life time of the hadronic fluctuation of the virtual photon [53], the energy loss of quarks before colorless objects are formed, the interactions with nuclear matter of the colorless objects, the evolution in time of the transverse size of the colorless objects, etc. Because of this interplay of various effects, which have different dependences on ν, Q^2 and x_{Bj}, it is difficult to test the theoretical ideas without detailed model predictions.

The y^* distribution of cascade hadrons, as given by $\mathrm{d}(\langle n \rangle_{\mu\mathrm{Xe}} - \langle n \rangle_{\mu\mathrm{D}})/\mathrm{d}y^*$, is shown for the LRG and SRG event samples in Figs. 23, 24. In the LRG event samples the multiplicity of hadrons from cascading is low over the whole y^* range. In the backward region this is due to the definition of a LRG event, which requires the absence of hadrons (except of grey tracks) in the rapidity gap. In the forward region the cascade process is known to contribute only little anyway. Abundant production of cascade hadrons is seen in the SRG event samples, and the size of the cascade effect is the same within the errors in the shadowing and non-shadowing region.

4.9 Evidence for a strong contribution of diffractive events in the LRG event samples

Compared to ordinary deep-inelastic events, diffractive events are characterized by lower average masses (m_X) and lower average multiplicities (n_X) of the diffractive system X [80, 32]. A comparison of the LRG and SRG events with respect to these quantities may therefore provide further evidence for the enrichment of the LRG samples with diffractive events. In the SRG events the "diffractive system" is defined as the hadronic system consisting of those observed hadrons that have rapidities beyond the rapidity region which corresponds to the rapidity gap required for the LRG events. Since only charged hadrons are accepted in the present experiment m_X and n_X are calculated using charged hadrons only.

Further quantities that will be compared are the charge (ch_X) of the diffractive system and the charged forward multiplicity (n_F). It should be noted that with the chosen lower limit of the rapidity gap size of 2 the minimum rapidity gap required for LRG events does not extend into the forward region, for any W in the present data sample.

In Fig. 25 the distributions of n_X, normalized to the number of entries, are shown for μXe scattering, in the shadowing and non-shadowing region. In each subfigure the LRG events are compared with the SRG events. In the VENUS model (Figs. 25c,d), which does not include diffractive processes, and which is assumed to describe non-diffractive scattering properly, no difference is seen between the LRG and SRG event samples. The experimental data, on the other hand (Figs. 25a,b), exhibit a clear shift of the distributions to lower values of n_X in the LRG event samples. This is clear evidence for a significant contribution of diffractive events in the LRG event samples, with a stronger effect in the low-x_{Bj} (sha) region. Qualitatively similar observations are made in μD scattering (Fig. 26).

The same data as in Figs. 25 and 26 are displayed also in Figs. 27 and 28, however, now in each subfigure the distributions in the shadowing and non-shadowing region are compared with each other. In the VENUS Monte Carlo data (Figs. 27c,d and 28c,d) the distributions in the shadowing region are shifted to higher values of n_X relative to the distribution in the non-shadowing region, both in μD and μXe scattering and both for the LRG and SRG events. The shift is due to the higher average W in the shadowing region, implying a larger available rapidity range and a larger average hadron multiplicity. In the experimental data (Figs 27a,b and 28a,b) the same kinematic effect is only clearly seen in the SRG event sample, while in the LRG event sample the two distributions nearly coincide. (Note that the problem of different average W does not arise in the comparison of the LRG with the SRG event samples in Figs. 25 and 26). This observation suggests again a strong contribution to the LRG event samples from diffractive events, for which $\langle n_X \rangle$ is expected to depend only weakly on W.

The behavior of the distributions for m_X and n_F (not shown) is qualitatively similar to that for n_X in Figs. 25 to 28. This can be seen in part from Table 8, in which the average values of these quantities are compiled for the various data samples. The strong contribution from diffractive scattering in the LRG sample for the shadowing region in μXe scattering is also reflected in the low value of $\langle ch_X \rangle$, which should be zero for diffractive events.

A lower limit on the amount of diffractive events in the LRG event samples is estimated from the plots in Figs. 25a,b and 26a,b in the following way. The distribution in a certain variable (say n_X) for a LRG event sample is a superposition of the distributions for diffractive and non-diffractive events. The shape of the latter distribution is assumed to be given by the distribution for the corresponding SRG event sample. This is suggested by the VENUS predictions in Figs. 25c,d and 26c,d, which show that the distributions for non-diffractive events are identical for the LRG and SRG event sample. A lower limit of the fraction of diffractive events is determined by renormalizing the distribution for the SRG event sample such that its tail ($n_X > 7$) coincides with the tail of the distribution for the LRG event sample, and then subtracting the renormalized SRG distribution from the LRG distribution. As the results from the n_X and m_X distributions were consistent within the errors, the amounts of SRG events to be subtracted were averaged. The resulting lower limits on the fraction of diffractive events, in the shadowing and non-shadowing region, for μD and μXe scattering, are compiled in Table 9.

By the above procedure one has determined only a lower limit on the fraction of diffractive events because it is assumed that the tail of the n_X (or m_X) distribution for the LRG event sample is completely given by non-diffractive events, while in reality there will be in addition a tail from diffractive events. As those tails ($n_X > 7$, $m_X > 4.5$ GeV) are expected to be small, the actual fractions of diffractive events will be close to the lower limits.

An essential point in estimating lower limits on the fraction of diffractive events is the assumption, that at fixed x_{Bj}, the n_X (or m_X) distributions for non-diffractive events are identical for the LRG and SRG event samples. This is suggested for both μD and μXe scattering by the VENUS Monte Carlo model, which does not include diffractive processes. It should be mentioned that for μD scattering in the Lund Monte Carlo model (LEPTO 6.1, JETSET 7.3) [88] the distributions for the LRG event samples are slightly shifted (although less strongly than for the experimental data) to lower values of n_X as compared to the SRG event samples. Such a behavior would imply lower values of the lower limits on the fraction of diffractive events than those listed in Table 9. In the Lund Monte Carlo model diffractive processes are not included explicitly either.

Diffractive channels in μ-nucleus scattering are studied in another analysis of the same experiment [89]. A characteristic feature of these channels is that most of the energy of the virtual photon is transferred to the system into which the virtual photon dissociates, giving rise to a kind of leading particle effect. An indication of this effect in μXe scattering is seen in Fig. 4 at large y* in the $n_g = 0$ subsample, in which the contribution from diffractive scattering should be enhanced.

5 Summary

In this analysis, hadron production in μXe interactions is studied and compared with that in μD and pXe scattering. The μXe and μD data are from the present experiment (E665), while the pXe data have been published by the NA5 collaboration. Most of the comparisons are done as a function of the number of grey tracks (protons in the momentum region from 200 to 600 MeV/c) in an event. In addition, in μXe scattering the comparison of hadron production between the shadowing ($x_{Bj} < 0.02$) and non-shadowing ($x_{Bj} > 0.02$) region is extensively discussed. The main results are:

- The average multiplicity $\langle n_g \rangle$ of grey tracks is significantly lower in μXe than in pXe scattering : $\langle n_g \rangle_{\mu\mathrm{Xe}} = 0.56 \pm 0.02, \langle n_g \rangle_{\mathrm{pXe}} = 2.53 \pm 0.08$.

- Also the average number of collisions with nucleons in the Xe nucleus $\langle \nu_c \rangle$ as calculated from the average (uncorrected) total hadronic net charge $\langle Q_T \rangle$, is significantly smaller in μXe (4.13 ± 0.15) than in pXe scattering (12.32 ± 0.32). The low values of both $\langle n_g \rangle_{\mu\mathrm{Xe}}$ and of $\langle \nu_c \rangle_{\mu\mathrm{Xe}}$ may be partially explained by the low number of projectile collisions $\langle \nu_{\mathrm{proj}} \rangle_{\mu\mathrm{Xe}}$ in μXe scattering: From the strength of shadowing of the cross section on Xe nuclei the average number of projectile collisions is estimated as $\langle \nu_{\mathrm{proj}} \rangle_{\mu\mathrm{Xe}} = 1.09 \pm 0.04, \langle \nu_{\mathrm{proj}} \rangle_{\mathrm{pXe}} = 3.24 \pm 0.13$.

- Grey tracks are a very efficient means for tagging events in which cascade interactions occur : the nuclear effects on hadrons are strongly enhanced in the sample of μXe events which contain grey tracks. The sample of μXe events without grey tracks resembles closely the μD event sample.

- The hadronic net charge is strongly correlated with n_g, the correlation being similar in μXe and pXe scattering. By fixing n_g one selects subsamples with slightly higher values of $\langle \nu_c \rangle$ in pXe than in μXe scattering.

- The Xe/D ratio $\overline{R}\,(n_g)$ of average charged multiplicities, integrated over the whole rapidity region, is essentially a function of $\langle \nu_{\mathrm{proj}}(n_g) \rangle$ in pXe, whereas it depends mainly on $\langle \nu_c \rangle$ in μXe scattering, where $\langle \nu_{\mathrm{proj}}(n_g) \rangle$ is close to 1.

- The variation of $R\,(n_g)$ with n_g in different rapidity regions reveals the characteristics of particle production on a nucleus :

  1. copious production of hadrons in the target fragmentation region, due to cascade interactions;
  2. in the central rapidity region : additional production of hadrons due to multiple projectile collisions in pXe scattering; only little additional hadron production in μXe scattering, as expected for $\langle \nu_{\mathrm{proj}} \rangle_{\mu\mathrm{Xe}} \approx 1$;

3. at large n_g, depletion of hadrons in the projectile fragmentation region, due to energy loss in projectile or cascade interactions. Note that in μXe scattering the large-n_g events constitute only a tiny fraction of all events. As compared to the pXe data, the μXe data exhibit a stronger depletion of fast hadrons than expected on the basis of the number of projectile collisions.

- From a comparison of the characteristics of the LRG (large-rapidity-gap) with those of the SRG (small-rapidity-gap) event samples, in the shadowing and non-shadowing region, it is concluded that the LRG event samples are enriched with diffractive events, both in μD and μXe scattering. This conclusion is supported by a comparison with the VENUS model, which is assumed to describe the behavior of non-diffractive processes properly.

- Lower limits on the fraction of diffractive events are determined. The limits are higher in the shadowing than in the non-shadowing region, and in the shadowing region they are higher for μXe than for μD scattering. These results support current models of nuclear shadowing in lepton-nucleus scattering, in which nuclear shadowing and diffractive scattering are closely related.

- In μXe scattering there is a clear dependence of hadron production on x_{Bj}, implying stronger nuclear effects in the hadronic system in the non-shadowing ($x_{Bj} > 0.02$) than in the shadowing ($x_{Bj} < 0.02$) region. This is in contrast to expectations, which are based on the distance within the nucleus available for cascading. After removal of the LRG (and thus of the diffractive) events hadron production is practically independent of x_{Bj}. This implies that cascading of hadrons, which is the dominant nuclear effect in the hadronic system, is very similar in the shadowing and non-shadowing region, when only the non-diffractive interactions are considered.

In conclusion, the main observations may be summarized as follows. Nuclear effects in the hadronic system are considerably smaller in μXe than in pXe scattering. Qualitatively this can be understood by the small average number $\langle\nu_{\mathrm{proj}}\rangle_{\mu\mathrm{Xe}}$ of projectile collisions in μXe scattering. Due to the low value of $\langle\nu_{\mathrm{proj}}\rangle_{\mu\mathrm{Xe}}$ the dominant mechanism for additional hadron production in μXe scattering is cascading. In the μD and μXe data clear evidence is found for a strong contribution from diffractive scattering. In μXe scattering the fraction of diffractive events is enhanced at low x_{Bj}, where shadowing of the cross section is observed. The diffractive events tend to dilute hadron production in the shadowing region. For the non-diffractive events the cascade effects in the μXe interaction are similar in the shadowing and non-shadowing region.

First experimental evidence is found for the close relation between nuclear shadowing and diffractive scattering in lepton-nucleus interactions.

Acknowledgements

We wish to thank all those personnel, both at Fermilab and the participating institutions, who have contributed to the success of this experiment. It is a pleasure to acknowledge the work of the scanning and measuring teams at our laboratories. We thank B. Leupold, P. Strube and M. Vidal for their excellent work in the production and processing of the streamer chamber data. We are grateful to B. Kopeliovich, N. Nikolaev and L. Stodolsky for many fruitful and enlightening discussions and for a critical reading of the manuscript. N. Nikolaev has drawn our attention to the importance of diffraction scattering, which has had a tremendous impact on this analysis.

This work was performed at the Fermi National Accelerator Laboratory, which is operated by Universities Research Association, Inc., under contract DE-AC02-76CHO3000 with the U.S. Department of Energy. The work of the University of California, San Diego was supported in part by the National Science Foundation, contract numbers PHY82-05900, PHY85-11584, and PHY88-10221; the University of Illinois at Chicago by NSF contract PHY88-11164; and the University of Washington by NSF contract numbers PHY83-13347 and PHY86-13003. The University of Washington was also supported by the U.S. Department of Energy. The work of Argonne National Laboratory was supported by the Department of Energy, Nuclear Physics Division, under Contract No. W-31-109-ENG-38. The Department of Energy, High Energy Physics Division, supported the work of Harvard University, the University of Maryland, the Massachussetts Institute of Technology under Contract No. DE-AC02-76ER03069, Northwestern University under Contract No. DE-FG02-91ER40684, and Yale University. The Albert-Ludwigs-Universität Freiburg and the University of Wuppertal were supported in part by the Bundesministerium für Forschung und Technologie. The work of the Institute for Nuclear Physics, Krakow, was supported in part by the Polish Committee for Scientific Research under grant No. 2P30204104. The work of J. Figiel was carried out as part of the European Community mobility action.

References

[1] K. Zalewski, Proc. of the Topical Meeting on Multiparticle Production on Nuclei at Very High Energies, Trieste, Italy (1976) 145, eds. G. Bellini et al., International Centre for Theoretical Physics, Trieste 1977

[2] A. Dar, J. Vary, Phys. Rev. **D6** (1972) 2412

[3] L. Hand et al., Acta Phys. Pol. **B9** (1978) 1087

[4] J.D. Bjorken, SLAC-PUB-1756 (1975)

[5] G.V. Davidenko et al., Nucl. Phys. **B135** (1978) 333

[6] A. Białas, W. Czyz, Nucl. Phys. **B137** (1978) 359

[7] J. Babecki, G. Nowak, Acta Phys. Pol. **B9** (1978) 401

[8] B. Andersson et al., Phys. Lett **B73** (1978) 343

[9] M.K. Hegab, J. Hüfner, Phys. Lett. **105B** (1981) 103

[10] N. Suzuki, Progr. of Theor. Phys. **67** (1982) 571

[11] M.K. Hegab, J. Hüfner, Nucl. Phys. **A384** (1982) 353

[12] K. Braune et al., Z. Phys. **C13** (1982) 191

[13] F. Verbeure, Proc. 14th Intern. Symp. on Multiparticle Dynamics, Granlibakken, Lake Tahoe, USA (1983), 947, eds. P. Yager, J.F. Gunion, World Scientific, Singapore 1984

[14] C. De Marzo et al., Phys. Rev. **D26** (1982) 1019

[15] C.D. Rees et al., Z. Phys. **C17** (1983) 95

[16] K. Braune et al., Z. Phys. **C17** (1983) 105

[17] C. De Marzo et al., Phys. Rev. **D29** (1984) 2476

[18] J.L. Bailly et al., Z Phys. **C35** (1987) 301

[19] D.H. Brick et al. Phys. Rev. **D39** (1989) 2484

[20] D.H. Brick et al., Phys. Rev. **D41** (1990) 765

[21] R.K. Shivpuri et al., Z. Phys. **C58** (1993) 419

[22] M.R. Adams et al., Phys. Rev. Lett. **68** (1992) 3266

[23] M.R. Adams et al., Phys. Lett. **B287** (1992) 375

[24] L. Stodolsky, Phys. Rev. Lett. **18** (1967) 135

[25] V.N. Gribov, Sov. Phys. JETP **29** (1969) 483

[26] N.N. Nikolaev et al., Phys. Lett. **B55** (1975) 397

[27] N.N. Nikolaev et al., Sov. J. Nucl. Phys. **B21** (1975) 227

[28] N.N. Nikolaev, Z. Phys. **C5** (1980) 291

[29] J.D. Bjorken, Contribution to the Festschrift of Jack Steinberger, K. Kleinknecht, T.D. Lee eds. ,p. 17 (1986).

[30] N.N. Nikolaev, B.G. Zakharov, Phys. Lett. **B260** (1991) 414

[31] N.N. Nikolaev, B.G. Zakharov, Z. Phys. **C49** (1991) 607

[32] N.N. Nikolaev, B.G. Zakharov, Z. Phys. **C53** (1992) 331

[33] B. Badełek et al., Nucl. Phys. **B370** (1992) 278

[34] L. Stodolsky, Phys. Lett. **B325** (1994) 505

[35] L. Hand et al., Z. Phys. **C1** (1979) 139

[36] M.R. Adams et al., Phys. Rev. **D50** (1994) 1836

[37] B. Pawlik, Ph.D. Thesis, Jagellonian University Cracow, 1982

[38] F. Dengler et al., Z. Phys. **C33** (1986) 187

[39] N.N. Nikolaev, et al., Forschungszentrum Jülich preprint KFA-IKP(TH)-1994-13, Juni 1994

[40] M. R. Adams et al., Nucl. Inst. and Meth. **A291** (1990) 533

[41] S. Söldner-Rembold, Ph.D. Thesis, Technische Universität München (1992), MPI report MPI-PhE/92-17 (October 1992)

[42] M.R. Adams et al., Z. Phys. **C61** (1994) 179

[43] G. Ingelman, T. Sjöstrand, LU TP 80-12, University of Lund (1980)

[44] T. Sjöstrand, Comp. Phys. Comm. **27** (1982) 243

[45] K. Werner und P. Koch, Z. Phys. **C47** (1990) 255

[46] K. Werner, CERN-TH-5682/90, Lectures presented at the Summer School on Phase Structures of Strongly Interacting Matter, Cape Town, South Africa (1990) p. 133

[47] K. Werner, Phys. Rep. **232** (1993) 87

[48] A. Bialas, W. Czyz, Phys. Lett. **B51** (1974) 179

[49] A. Gurtu et al., Pramana **3** (1974) 311

[50] W. Busza et al., Phys. Rev. Lett. **34** (1975) 836

[51] A.S. Carroll et al., Phys. Lett. **80B** (1979) 319

[52] V. Flaminio et al., CERN-HERA 79-03 (1979)

[53] T.H. Bauer et al., Rev. Mod. Phys. **50** (1978) 261

[54] L.L. Frankfurt, M. Strikman, Phys. Rep. **160** (1988) 235

[55] L.L. Frankfurt et al., Nucl. Phys. **B316** (1989) 340

[56] Alma Ata-Leningrad-Moscow-Tashkent collaboration, preprint 9, Moscow (1974)

[57] M.A. Faessler et al., Nucl. Phys. **B157** (1979) 1

[58] F. Roesler, C.B.A. McCusker, Nuovo Cim. **10** (1953) 127

[59] I.Z. Artykov et al., Nucl. Phys. **B6** (1968) 11

[60] A. Gurtu et al., preprint TIFR-DC-6 (1974); Phys. Lett. **50B** (1974) 391

[61] B. Andersson, I. Otterlund, Nucl. Phys. **B99** (1975) 425

[62] E.M. Friedländer, Lett. Nuovo Cim. **9** (1974) 349

[63] P.M. Fishbane et al., Phys. Rev. **D9** (1974) 168

[64] P.M. Fishbane, J.S. Trefil, Phys. Lett. **51B** (1974) 139

[65] J. Calucci et al., Phys. Rev. **D10** (1974) 1468

[66] J.R. Florian et al., Phys. Rev. **D13** (1976) 558

[67] A. Capella et al., Phys. Lett. **81B** (1979) 68; Z. Phys. **C10** (1981) 249; Phys. Lett. **114B** (1982) 450

[68] W.Q. Chao et al., Phys. Rev. Lett. **44** (1980) 518

[69] C.B. Chiu et al., Phys. Rev. **D25** (1982) 2911

[70] K. Fiałkowski, W. Kittel, Rep. Prog. Phys. **46** (1983) 1283

[71] W. Busza, Acta Phys. Pol., **B8** (1977) 333

[72] N.N. Nikolaev, Phys. Lett. **60B** (1976) 363

[73] A. Bialas and L. Stodolsky, Acta Phys. Pol. **B7** (1976) 845

[74] A. Bialas, Proc. 13th Intern. Symp. on Multiparticle Dynamics, Volendam, The Netherlands (1982) 328, eds. W. Kittel et al., World Scientific, Singapore 1983

[75] N. Pavel, Internal EMC report, EMC/88/2 (1988)

[76] L.W. Mo, Y.S. Tsai, Rev. Mod. Phys. **41** (1969) 205

[77] L.L. Frankfurt et al., Leningrad Institute of Nuclear Physics preprint 329 (1977)

[78] B.Z. Kopeliovich et al., Phys. Lett. **B309** (1993) 179

[79] B.Z. Kopeliovich et al., Phys. Lett. **B324** (1994) 469

[80] K. Goulianos, Phys. Rep. **101** (1983) 169

[81] M. Derrick et al., Phys. Lett. **B315** (1993) 481

[82] A. De Roeck, Proc. XVI Intern. Europhysics Conf. on High Energy Physics, Marseille, France (1993), p. 791, eds. J. Carr, M. Perrottet, Editiones Frontiéres, Gif-sur-Yvette 1994

[83] M. Derrick et al., Observation of Jet Production in Deep Inelastic Scattering with a Large Rapidity Gap at HERA, DESY 94-063 (1994)

[84] B.Z. Kopeliovich, Phys. Lett. **243B** (1990) 141

[85] B.Z. Kopeliovich, J. Nemchik, Dubna preprint E2-91-150 (1991)

[86] B. Kopeliovich, J. Nemchik, Istituto Nazionale Fisica Nucleare preprint INFN-ISS 91/3, May 1991

[87] B. Kopeliovich, preprint LPTHE 93-16, Talk presented at the Workshop on Future Directions in Particle and Nuclear Physics with Multi-GeV Hadronic Beam Facilities, Brookhaven, USA (1993)

[88] G. Ingelman, Proceedings of the Workshop 'Physics at HERA', Hamburg, Oct. 1991, W. Buchmüller, G. Ingelman (eds.), Vol. 3, p. 1366;
T. Sjöstrand, A Manual to the Lund Monte Carlo for Jet Fragmentation and e^+e^- Physics, JETSET version 7.3, June 1991; T. Sjöstrand, Comput. Phys. Commun. **39** (1986) 347; **43** (1987) 367

[89] M.R. Adams et al., Measurement of Nuclear Transparencies from Exclusive ρ^0 Meson Production in Muon-Nucleus Scattering at 470 GeV, paper submitted to Phys. Rev. Lett. (1994)

	μD	μXe
efficiency of the identification of protons in the momentum region 200 to 600 MeV/c	0.75	0.75
contamination of grey tracks sample by pions and kaons	0.43	0.15
acceptance of positive particles in the forward hemisphere	0.78	0.81
acceptance of negative particles in the forward hemisphere	0.73	0.73
acceptance of positive particles in the backward hemisphere	0.96	0.82
acceptance of negative particles in the backward hemisphere	0.96	0.94

Table 1: Parameters used in the Monte Carlo program to simulate the identification efficiency and the acceptance of hadrons in the experiment.

	μXe			pXe	ratio $\frac{\text{pXe total}}{\mu\text{Xe total}}$
	total	shadowing region A	non-shadowing region B	total	
$\langle\nu_{\text{proj}}\rangle$	(1.09±0.04)	1.19±0.05	(∼ 1.0)	3.24±0.13	2.97±0.16
$\langle n_g\rangle$	0.56±0.02	0.49±0.03	0.61±0.03	2.53±0.08	4.52±0.22
$\langle Q_T\rangle$	1.70±0.06	1.49±0.09	1.85±0.08	6.05±0.14	
$\langle\nu_c\rangle$	4.13±0.15*	3.62±0.22	4.50±0.19	12.32±0.32	2.98±0.13
$\langle n_B\rangle_{\text{Xe}} - \langle n_B\rangle_{\text{D}}$	1.78±0.09	1.63±0.16	1.95±0.12	9.02±0.26	5.07±0.30
$\langle Q_T\rangle_{\text{Xe}} - \langle Q_T\rangle_{\text{D}}$	1.11±0.06	0.89±0.09	1.28±0.09	4.16±0.14	3.75±0.24
$\langle n_g\rangle/\langle\nu_{\text{proj}}\rangle$	(0.51±0.03)	0.41±0.03	(0.61±0.03)	0.78±0.04	

*) This is $\langle\nu_c\rangle$ as calculated from the uncorrected value of $\langle Q_T\rangle$ (line 3) using (9). The corresponding corrected value is 5.37±0.41 [42].

Table 2: Quantities expected to be sensitive to nuclear effects as measured in μXe and pXe scattering. In the μXe reaction the measurements are given for the total kinematic range defined by (3) and separately for the shadowing ($x_{Bj} < 0.02$) and non-shadowing ($x > 0.02$) region.

	a_Q	b_Q
μXe	0.86±0.05	1.53±0.06
pXe	1.85±0.06	1.72±0.04

Table 3: Parameter values a_Q and b_Q from fits of the expression $(a_Q + b_Q \cdot n_g)$ to the data points of $\langle Q_T \rangle$ in μXe and pXe scattering (Fig. 6a).

	charged	positive	negative
μXe	0.32±0.02	0.50±0.02	0.10±0.02
pXe	0.42±0.02	0.56±0.02	0.23±0.02

Table 4: Values of the slope parameter b from fits of the expression $R = a + b \cdot n_g$ to the data points in Fig. 8.

target fragmentation region	central region	projectile fragmentation region
$y^* < -1.0$	$-0.5 < y^* < 0.5$	$y^* > 2.0$

Table 5: Definition, in terms of the center of mass rapidity y^*, of the target fragmentation, central and projectile fragmentation regions used in Fig. 10.

	total sample	$x_{Bj} < 0.02$ (shadowing region A)	$x_{Bj} > 0.02$ (non-shadowing region B)	$x_{Bj} < 0.02$ $W < 22$ GeV (shadowing region A′)	$x_{Bj} > 0.02$ $W > 13$ GeV (non-shadowing region B′)
range in x_{Bj}	0.002 - 0.30	0.002 - 0.02	0.02 - 0.30	0.002 - 0.02	0.02 - 0.30
$\langle x_{Bj} \rangle$	0.044	0.0095	0.068	0.011	0.055
range in Q^2(GeV^2)	1 - 100	1 - 14	1 - 100	1 - 10	4 - 100
$\langle Q^2 \rangle$ (GeV^2)	10.0	3.89	14.3	3.64	17.1
range in ν(GeV)	50 - 400	50 - 400	50 - 400	50 - 275	75 - 400
$\langle \nu \rangle$ (GeV)	172.1	233.7	128.7	177.2	175.5
range in W(GeV)	8 - 28	8 - 28	8 - 28	8 - 22	13 - 28
$\langle W \rangle$ (GeV)	17.0	20.5	14.5	17.9	17.3
no. of events	1999	826	1173	495	636

Table 6: Ranges of x_{Bj}, Q^2, ν and W covered by the total, shadowing and non-shadowing data samples, in μXe scattering.

	shadowing region A	non-shadowing region B	shadowing region A′	non-shadowing region B′
$\langle Q_T \rangle_{\mu \mathrm{Xe}}$	1.49 ± 0.09	1.85 ± 0.08	1.51 ± 0.11	1.90 ± 0.11
$\langle n_g \rangle_{\mu \mathrm{Xe}}$	0.49 ± 0.03	0.61 ± 0.03	0.49 ± 0.04	0.62 ± 0.04
$\langle n_B \rangle_{\mu \mathrm{Xe}} - \langle n_B \rangle_{\mu \mathrm{D}}$	1.63 ± 0.16	1.95 ± 0.12	1.65 ± 0.19	2.08 ± 0.16
$\langle Q_T \rangle_{\mu \mathrm{D}}$	0.60 ± 0.03	0.57 ± 0.03	0.60 ± 0.04	0.62 ± 0.04

Table 7: Comparison of $\langle Q_T \rangle_{\mu \mathrm{Xe}}$, $\langle Q_T \rangle_{\mu \mathrm{D}}$, $\langle n_g \rangle_{\mu \mathrm{Xe}}$ and $(\langle n_B \rangle_{\mu \mathrm{Xe}} - \langle n_B \rangle_{\mu \mathrm{D}})$ between the shadowing and non-shadowing regions.

	SRG		LRG	
	shadowing region A	non-shadowing region B	shadowing region A	non-shadowing region B
μXe				
fraction of events	0.71±0.02	0.81±0.01	0.29±0.02	0.19±0.01
$\langle n_X \rangle$	6.79±0.14	5.26±0.09	4.15±0.21	4.26±0.19
$\langle m_X \rangle$ (GeV)	3.95±0.10	2.61±0.06	2.29±0.14	1.96±0.10
$\langle ch_X \rangle$	0.43±0.08	0.36±0.05	0.06±0.09	0.37±0.09
$\langle n_F \rangle$	4.12±0.09	3.56±0.06	3.00±0.15	3.23±0.14
no. of events	590	946	236	227
μD				
fraction of events	0.73±0.01	0.75±0.01	0.27±0.01	0.25±0.01
$\langle n_X \rangle$	5.85±0.07	4.78±0.05	4.60±0.10	4.14±0.09
$\langle m_X \rangle$ (GeV)	3.68±0.05	2.58±0.04	2.71±0.07	2.19±0.06
$\langle ch_X \rangle$	0.29±0.04	0.27±0.03	0.24±0.05	0.28±0.04
$\langle n_F \rangle$	3.74±0.05	3.38±0.04	3.32±0.07	3.11±0.07
no. of events	2084	2391	785	811

Table 8: Average values of various quantities for the SRG and LRG event samples in the shadowing and non-shadowing region, for μXe and μD scattering. n_X, m_X and ch_X are the charged hadron multiplicity, the effective mass (calculated using charged hadrons only) and the charge of the 'diffractive system'; n_F is the multiplicity of charged hadrons in the forward region.

	shadowing region A		non-shadowing region B	
	μD	μXe	μD	μXe
$(\text{diffractive/LRG})_{\text{min}}$	0.44±0.06	0.61±0.07	0.32±0.09	0.49±0.13
$(\text{diffractive/total})_{\text{min}}$	0.12±0.02	0.18±0.03	0.08±0.03	0.09±0.03

Table 9: Lower limits on the fraction of diffractive events in the LRG and total event sample, in the shadowing ($x_{Bj} < 0.02$) and non-shadowing ($x_{Bj} > 0.02$) region of μD and μXe scattering.

Figure 1: Diagrams for elastic $\gamma^* A$ scattering. a) single scattering, b) double scattering term.

Figure 2: Average total hadronic net charge $\langle Q_T \rangle$, average number of grey tracks $\langle n_g \rangle$ and difference of average charged backward multiplicities $\langle n_B \rangle_{\mu \mathrm{Xe}} - \langle n_B \rangle_{\mu \mathrm{D}}$ in μXe and μD scattering as a function of the leptonic energy transfer ν. The lines represent the predictions of the VENUS model.

Figure 3: Average hadronic net charge $\mathrm{d}\langle Q \rangle / \mathrm{d}y^*$ as a function of y^*, in μD events and in μXe events with $(n_g \neq 0)$ and without $(n_g = 0)$ grey tracks.

Figure 4: Multiplicity ratio $R = \langle n \rangle_{\mu \mathrm{Xe}} / \langle n \rangle_{\mu \mathrm{D}}$ as a function of y^*, for all charged and for positive and negative hadrons, for μXe events with $(n_g \neq 0)$ and without $(n_g = 0)$ grey tracks.

Figure 5: Multiplicity distribution $P(n_g)$ of grey tracks for μXe and pXe scattering. The lines represent the predictions of the VENUS model.

Figure 6: Average hadronic net charge as a function of the number n_g of grey tracks for μXe and pXe scattering, in the total rapidity region $(\langle Q_T \rangle)$ and in the backward $(\langle Q_B \rangle)$ and forward $(\langle Q_F \rangle)$ hemispheres. The lines represent the predictions of the VENUS model.

Figure 7: (a) Multiplicity ratio $\overline{R}(n_g)$ for charged hadrons as a function of the number n_g of grey tracks, in μXe and pXe scattering. The lines represent (13), using $\langle \nu_{\mathrm{proj}}(n_g) \rangle$ from Fig. 7b. (b) Estimated average number of projectile interactions $\langle \nu_{\mathrm{proj}}(n_g) \rangle$ as a function of the number n_g of grey tracks for μXe (solid line) and pXe (dotted line) scattering.

Figure 8: Multiplicity ratio $R(n_g)$ as a function of the number n_g of grey tracks for all charged, for positive and negative hadrons, in μXe and pXe scattering. The lines represent the predictions of the VENUS model.

Figure 9: Multiplicity ratio $R(n_g)$ for charged hadrons as a function of the number n_g of grey tracks for the backward and forward hemisphere, in μXe and pXe scattering. The lines represent the predictions of the VENUS model.

Figure 10: Multiplicity ratio $R(n_g)_{\mu \mathrm{Xe}}$ (full circles) and $R(n_g)_{\mathrm{pXe}}$ (open triangles) as a function of the number n_g of grey tracks. The plots are for all charged, for positive and negative hadrons, and for three rapidity intervals (target, central, projectile). The lines are the results of straight-line fits to the data points.

Figure 11: Multiplicity distribution $P(n_g)$ of grey tracks, for the shadowing and non-shadowing region in μXe scattering. The lines represent the predictions of the VENUS model.

Figure 12: Average hadronic net charge as a function of n_g, in the total rapidity range and in the backward and forward hemispheres, for the shadowing and non-shadowing region in μXe scattering. The lines represent the predictions of the VENUS model.

Figure 13: Multiplicity ratio $R(n_g)_{\mu\mathrm{Xe}}$ as a function of n_g, for all charged and for positive and negative hadrons, in the shadowing and non-shadowing region. The lines represent the predictions of the VENUS model.

Figure 14: Average hadronic net charge $\mathrm{d}\langle Q\rangle/\mathrm{d}y^*$ as a function of y^*, for the shadowing and non-shadowing region in μD (a)) and μXe (b)) scattering.

Figure 15: Difference of average multiplicities $\mathrm{d}(\langle n\rangle_{\mu\mathrm{Xe}} - \langle n\rangle_{\mu\mathrm{D}})/\mathrm{d}y^*$ in μXe and μD scattering as a function of y^* for all charged (a)), for positive (b)) and for negative (c)) hadrons, in the shadowing and non-shadowing region.

Figure 16: $\langle Q_T\rangle_{\mu\mathrm{Xe}}$, $\langle Q_T\rangle_{\mu\mathrm{D}}$, $\langle n_g\rangle_{\mu\mathrm{Xe}}$ and $\langle n_B\rangle_{\mu\mathrm{Xe}} - \langle n_B\rangle_{\mu\mathrm{D}}$ as a function of x_{Bj}. The lines represent the predictions of the VENUS model.

Figure 17: $\langle Q_T\rangle_{\mu\mathrm{Xe}}$, $\langle Q_T\rangle_{\mu\mathrm{D}}$, $\langle n_g\rangle_{\mu\mathrm{Xe}}$ and $\langle n_B\rangle_{\mu\mathrm{Xe}} - \langle n_B\rangle_{\mu\mathrm{D}}$ as a function of ν, in the shadowing and non-shadowing region. The lines represent the predictions of the VENUS model.

Figure 18: $\langle Q_T\rangle_{\mu\mathrm{Xe}}$, $\langle Q_T\rangle_{\mu\mathrm{D}}$, $\langle n_g\rangle_{\mu\mathrm{Xe}}$ and $\langle n_B\rangle_{\mu\mathrm{Xe}} - \langle n_B\rangle_{\mu\mathrm{D}}$ as a function of Q^2, in the shadowing and the non-shadowing region.

Figure 19: Fraction of events with a rapidity gap greater than Δy^* as a function of Δy^*, in μD and μXe scattering. The lines represent the predictions of the VENUS model.

Figure 20: Fraction of events with a rapidity gap greater than Δy^* as a function of Δy^*, in the shadowing and non-shadowing region, for μD and μXe scattering. The lines represent the predictions of the VENUS model.

Figure 21: Fraction of LRG events as a function of x_{Bj} in μD and μXe scattering. The lines represent the predictions of the VENUS model.

Figure 22: $\langle Q_T \rangle_{\mu \mathrm{Xe}}$, $\langle n_g \rangle_{\mu \mathrm{Xe}}$ and $\langle n_B \rangle_{\mu \mathrm{Xe}} - \langle n_B \rangle_{\mu \mathrm{D}}$ as a function of x_{Bj} for the SRG and LRG event samples. The lines represent the predictions of the VENUS model.

Figure 23: Difference of average multiplicities $\mathrm{d}(\langle n \rangle_{\mu \mathrm{Xe}} - \langle n \rangle_{\mu \mathrm{D}})/\mathrm{d}y^*$ in μXe and μD scattering as a function of y^*, for the LRG event samples in the shadowing (sha) and non-shadowing (nsh) region.

Figure 24: Difference of average multiplicities $\mathrm{d}(\langle n \rangle_{\mu \mathrm{Xe}} - \langle n \rangle_{\mu \mathrm{D}})/\mathrm{d}y^*$ in μXe and μD scattering as a function of y^*, for the SRG event samples in the shadowing (sha) and non-shadowing (nsh) region.

Figure 25: Distribution of the charged hadron multiplicity n_X of the 'diffractive system', in the shadowing (sha, a) and c)) and non-shadowing (nsh, b) and d)) region of μXe scattering. In each subfigure the SRG event sample is compared with the LRG event sample. a) and b) are for the experimental data, c) and d) for the VENUS Monte Carlo data. The lines are drawn to guide the eye.

Figure 26: Distribution of the charged hadron multiplicity n_X of the 'diffractive system', in the shadowing (sha, a) and c)) and non-shadowing (nsh, b) and d)) region of μD scattering. In each subfigure the SRG event sample is compared with the LRG event sample. a) and b) are for the experimental data, c) and d) for the VENUS Monte Carlo data. The lines are drawn to guide the eye.

Figure 27: Distribution of the charged hadron multiplicity n_X of the 'diffractive system', for the LRG (a) and c)) and SRG (b) and d)) event samples in μXe scattering. In each subfigure the shadowing region (sha) is compared with the non-shadowing region (nsh). a) and b) are for the experimental data, c) and d) for the VENUS Monte Carlo data. The lines are drawn to guide the eye.

Figure 28: Distribution of the charged hadron multiplicity n_X of the 'diffractive system', for the LRG (a) and c)) and SRG (b) and d)) event samples in μD scattering. In each subfigure the shadowing region (sha) is compared with the non-shadowing region (nsh). a) and b) are for the experimental data, c) and d) for the VENUS Monte Carlo data. The lines are drawn to guide the eye.

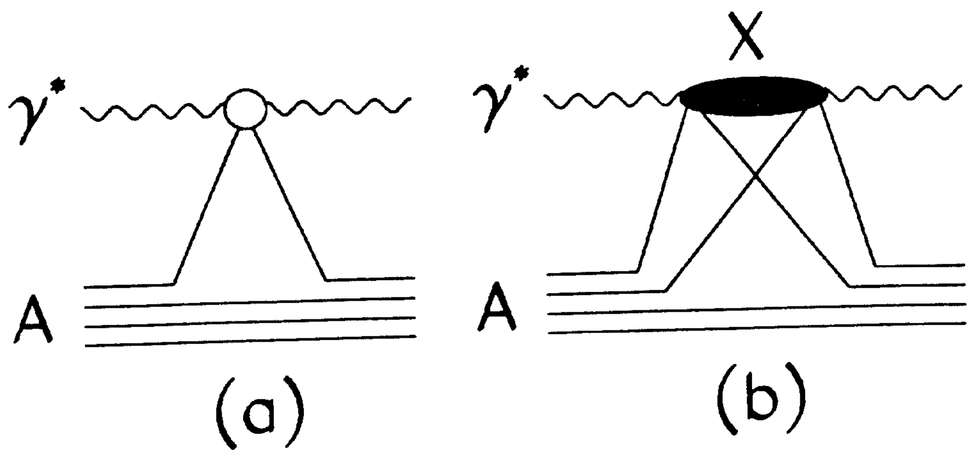

Fig. 1

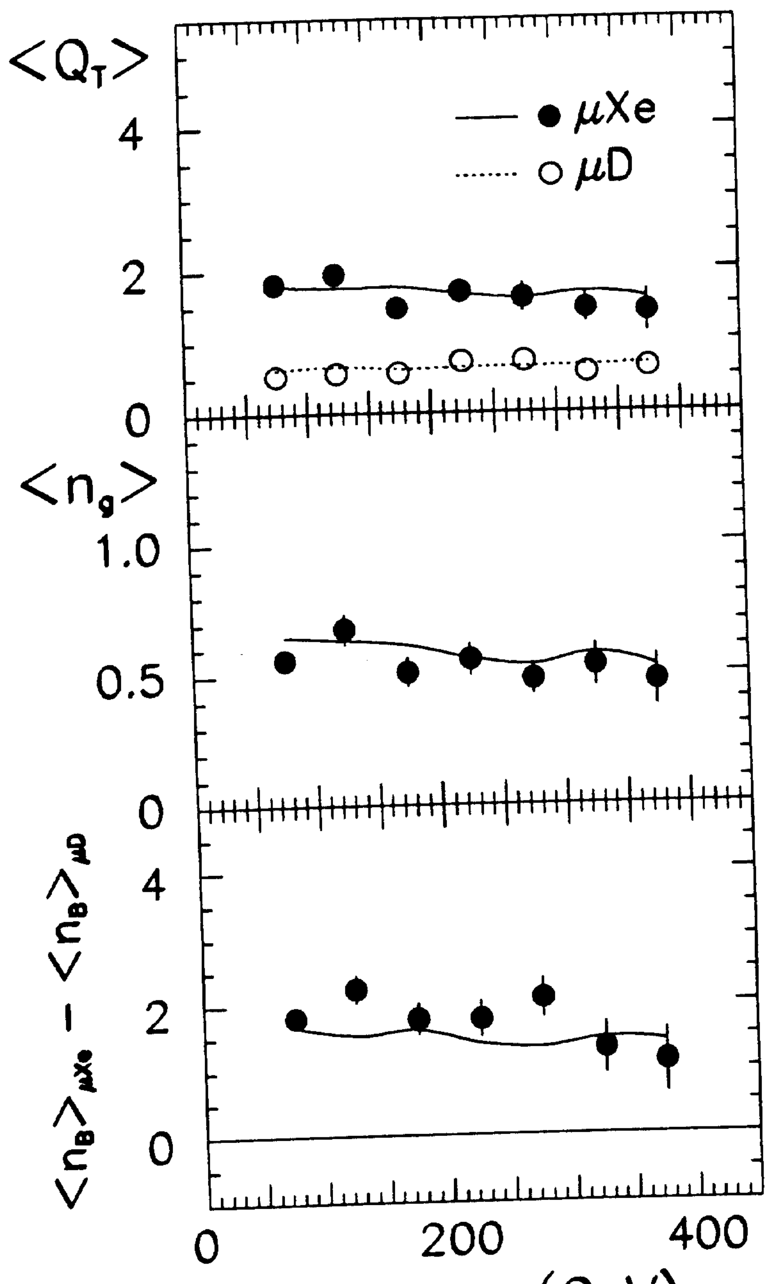

Fig. 2

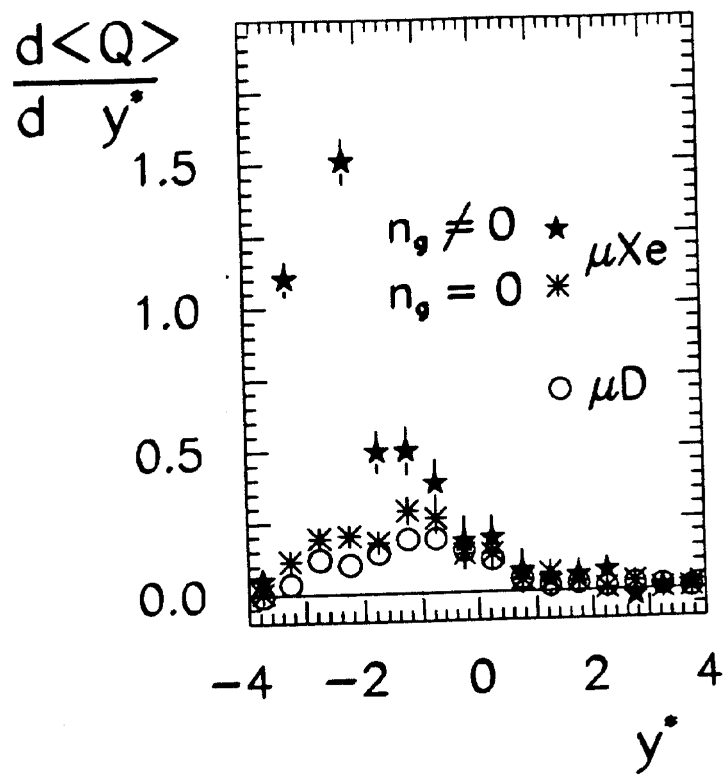

$\frac{d\langle Q\rangle}{d\ y^*}$
1.5
1.0
0.5
0.0
$n_g \neq 0$
$n_g = 0$
μXe
μD
−4
−2
0
2
4
y^*

Fig. 3

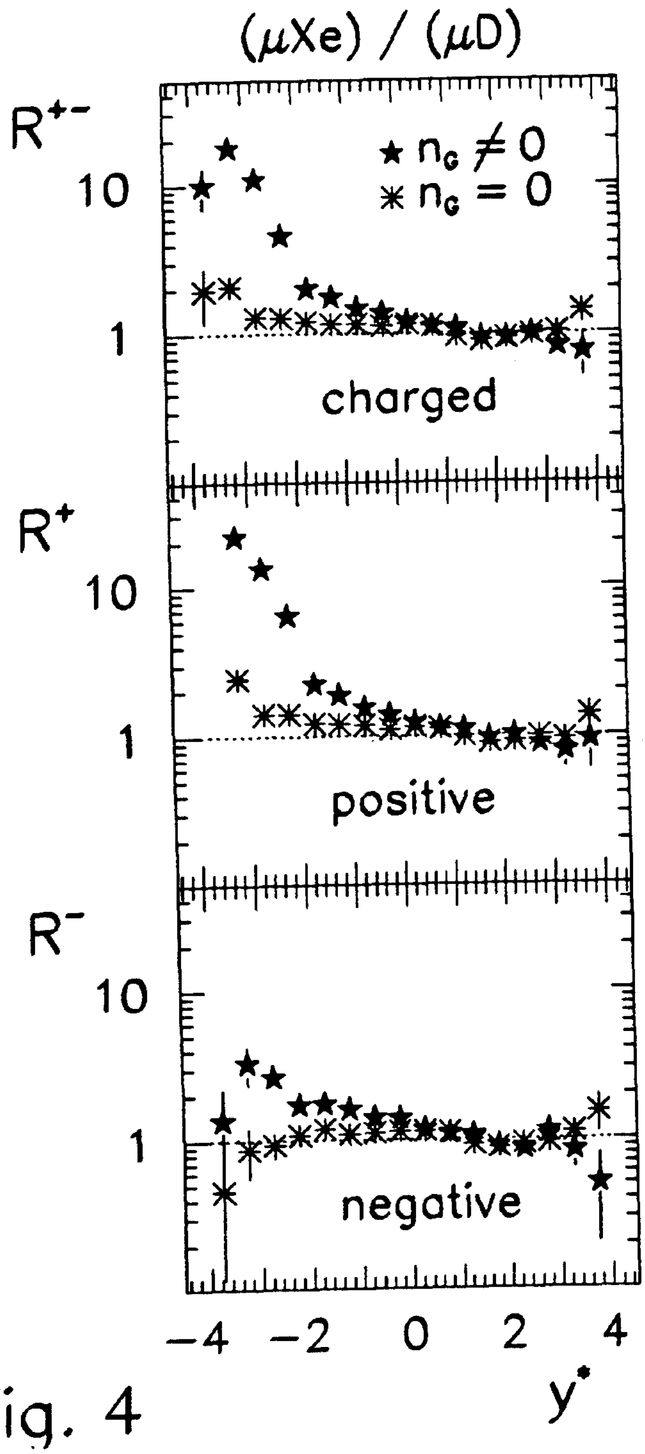
(μXe) / (μD)
R+-
10
1
n_G ≠ 0
n_G = 0
charged
R+
10
1
positive
R-
10
1
negative
-4 -2 0 2 4
y*

Fig. 4

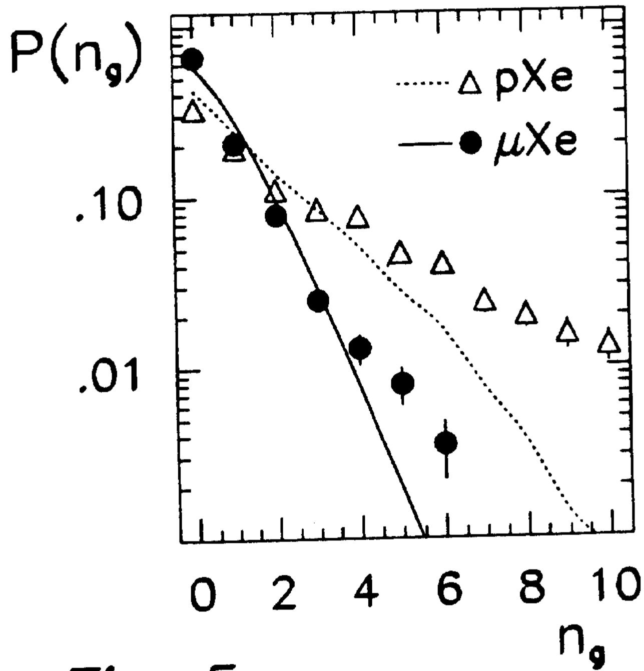

Fig. 5

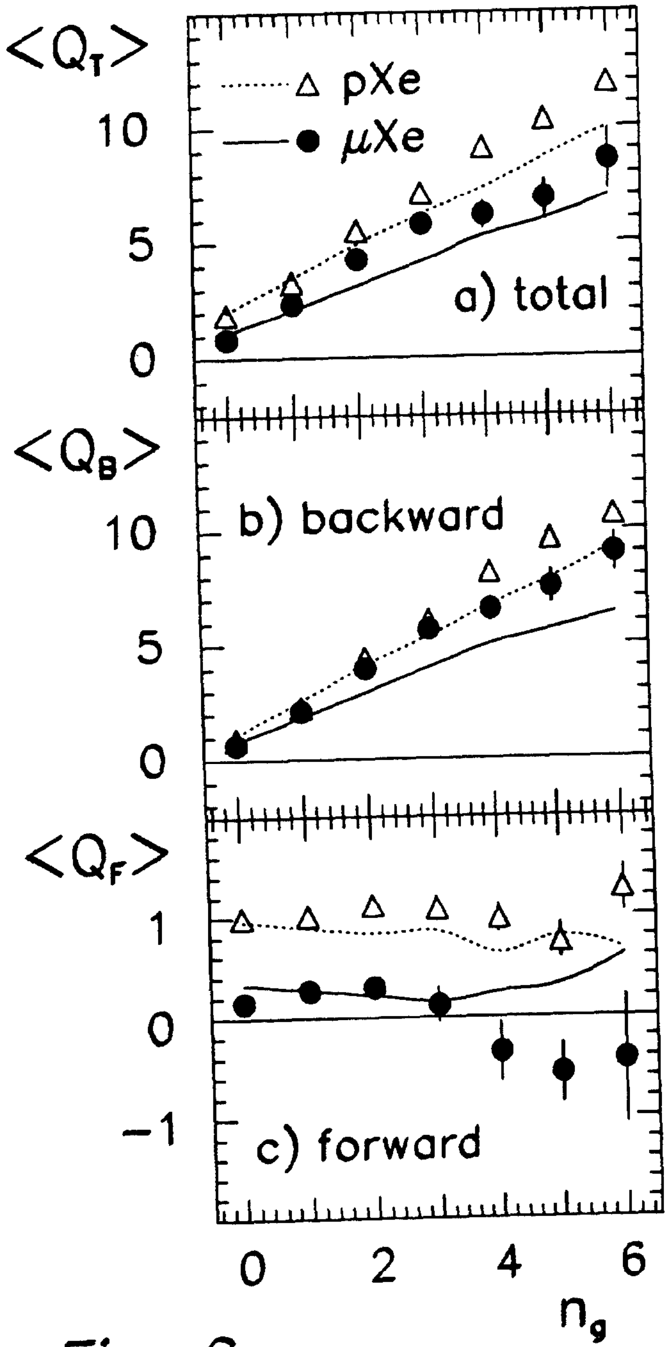

<QT>
pXe
μXe
10
5
0
a) total
<QB>
b) backward
10
5
0
<QF>
1
0
−1
c) forward
0
2
4
6
ng

Fig. 6

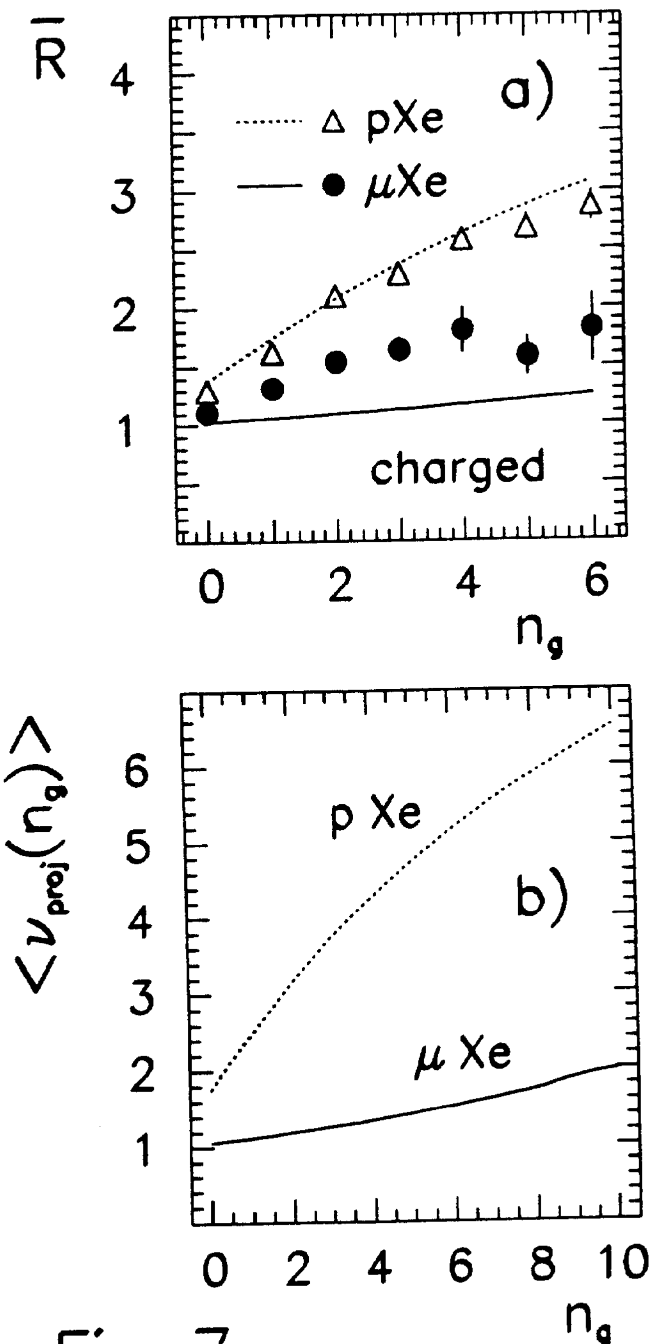

$\bar{R}$
4
3
2
1
a)
pXe
μXe
charged
0
2
4
6
n_g
$\langle \nu_{proj}(n_g) \rangle$
6
5
4
3
2
1
p Xe
b)
μ Xe
0
2
4
6
8
10
n_g

Fig. 7

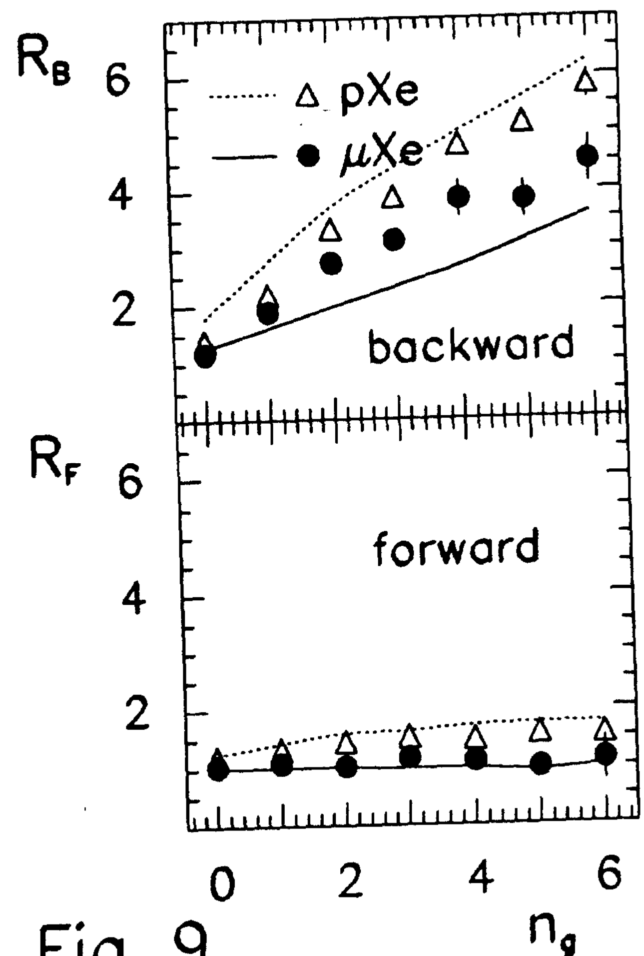

Fig. 9

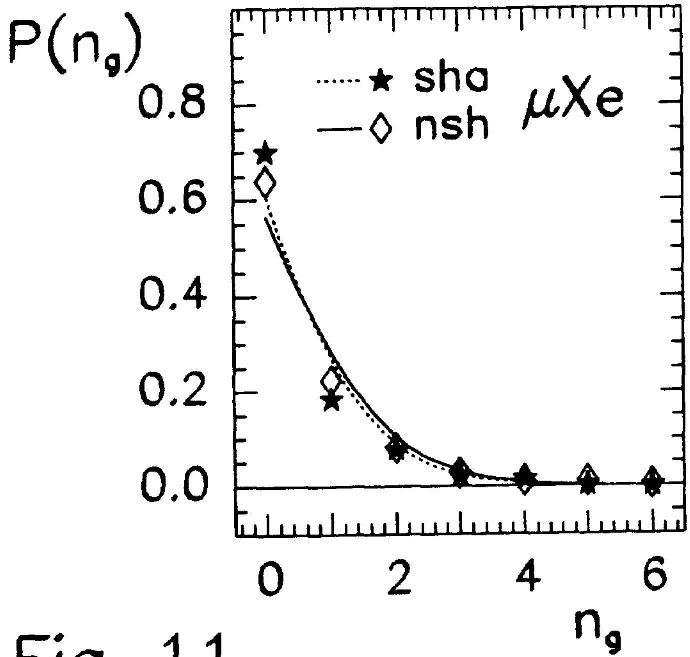

Fig. 11

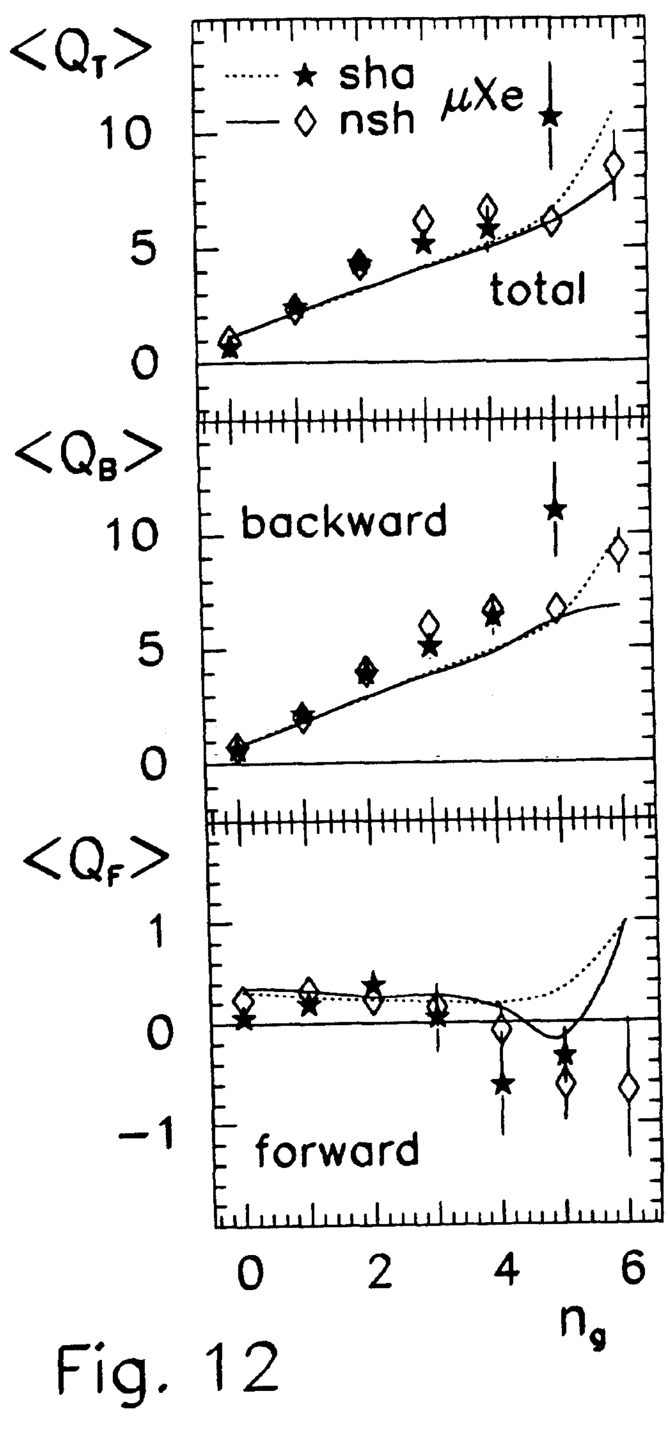

<QT>
sha
nsh
μXe
10
5
0
total
<QB>
backward
10
5
0
<QF>
1
0
−1
forward
0
2
4
6
n_g

Fig. 12

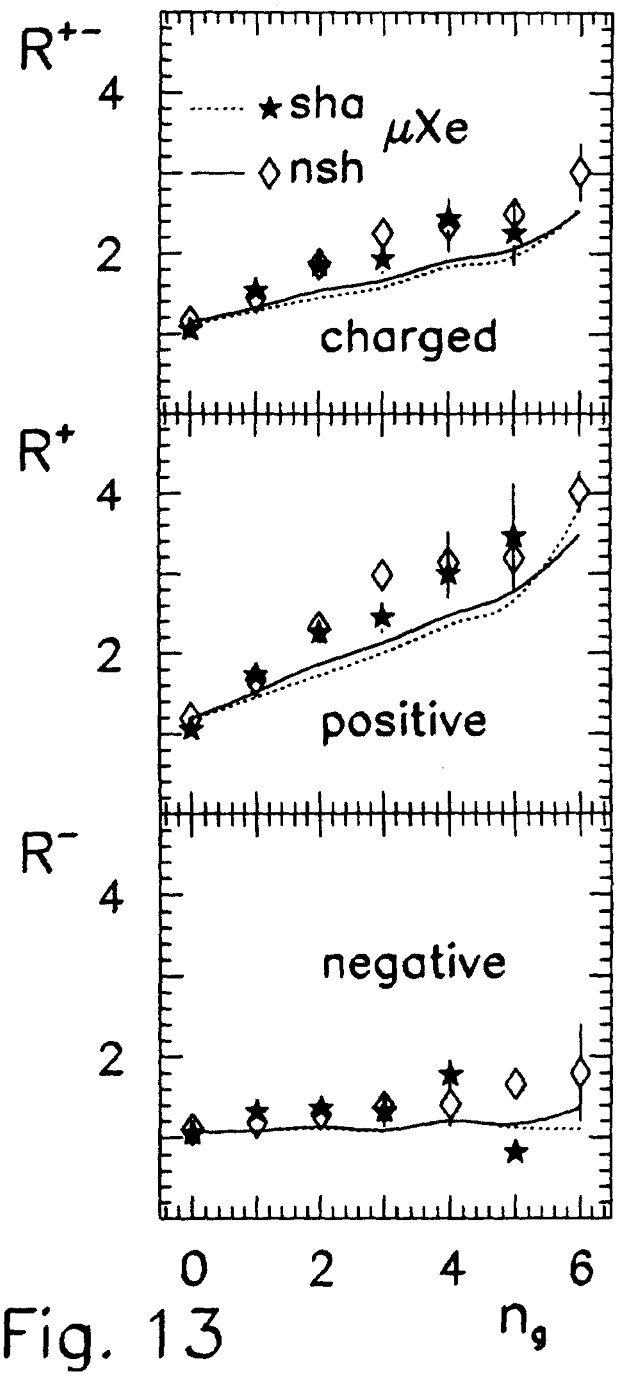

Fig. 13

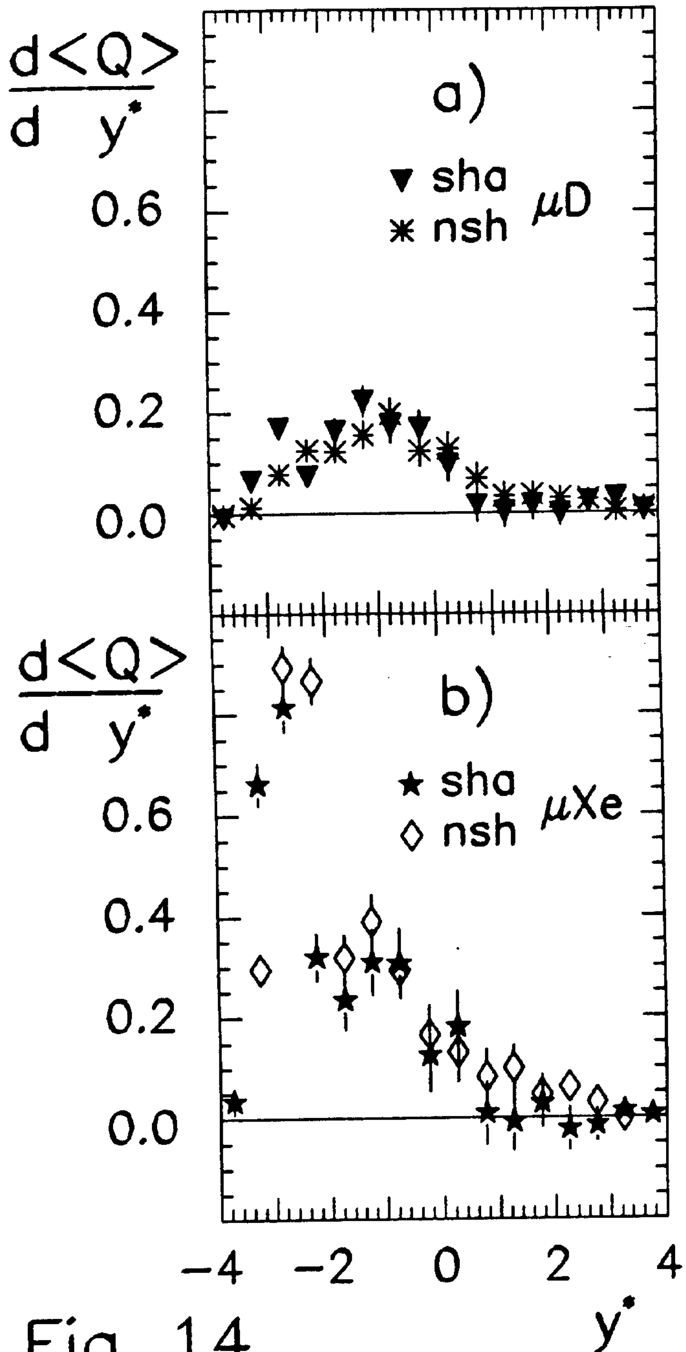

Fig. 14

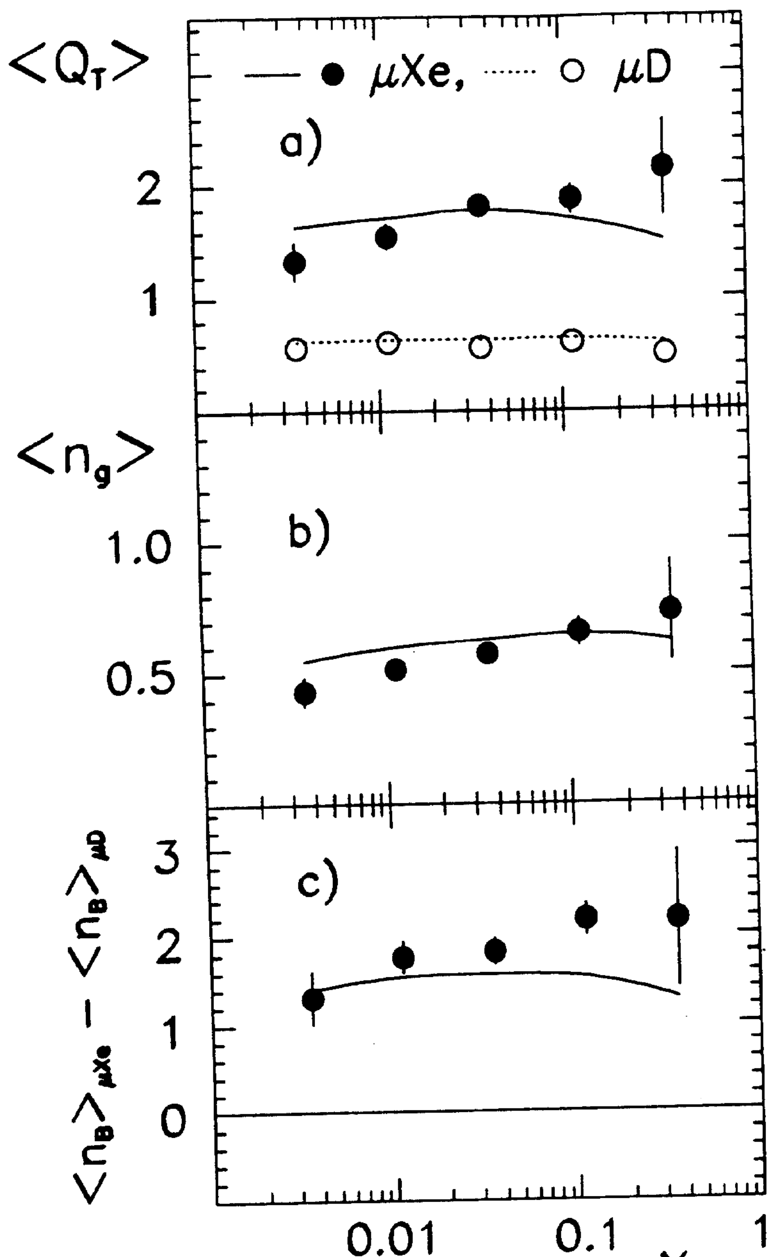

$\langle Q_T \rangle$
μXe, μD
a)
2
1
$\langle n_g \rangle$
b)
1.0
0.5
$\langle n_B \rangle_{\mu Xe} - \langle n_B \rangle_{\mu D}$
c)
3
2
1
0
0.01
0.1
1
X_{Bj}

Fig. 16

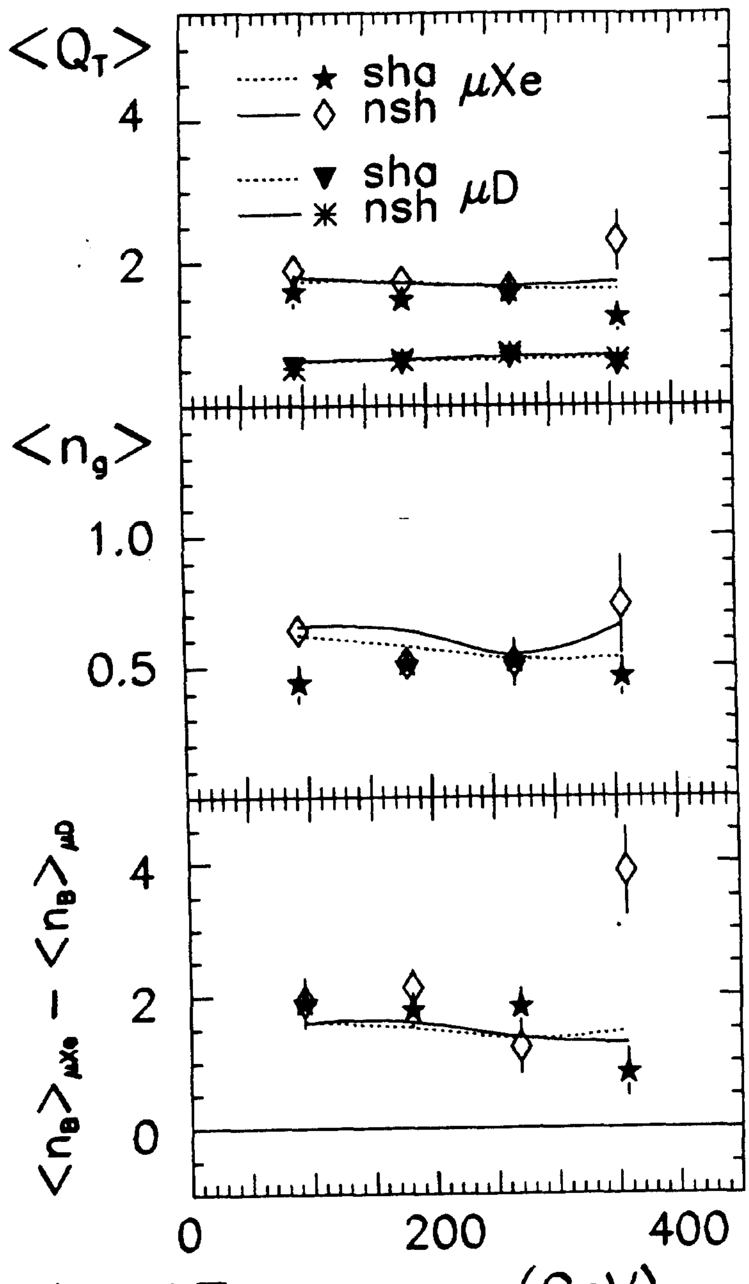
$\langle Q_T \rangle$
sha
nsh
μXe
sha
nsh
μD
$\langle n_g \rangle$
$\langle n_B \rangle_{\mu Xe} - \langle n_B \rangle_{\mu D}$
ν (GeV)

Fig. 17

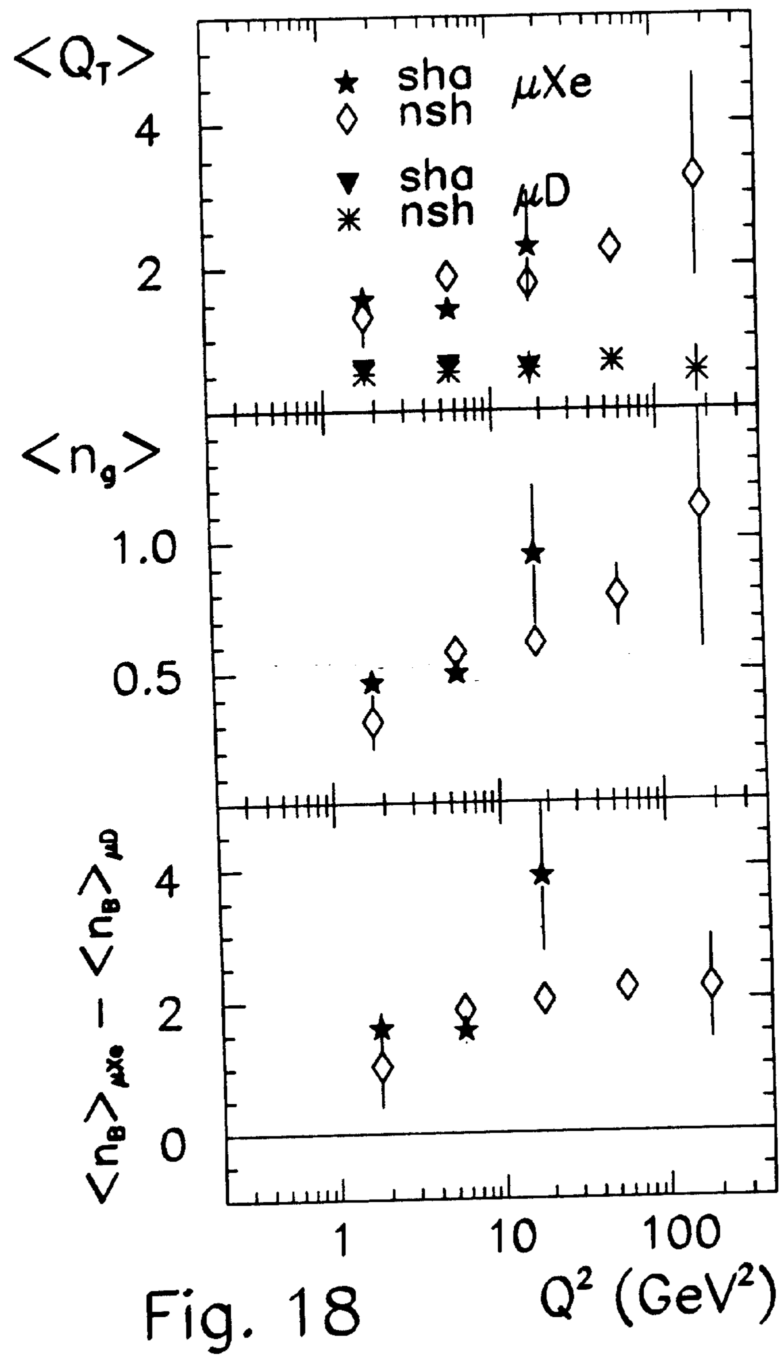

<QT>
sha
nsh
μXe
sha
nsh
μD
4
2
<ng>
1.0
0.5
<nB>μXe − <nB>μD
4
2
0
1
10
100
Q² (GeV²)

Fig. 18

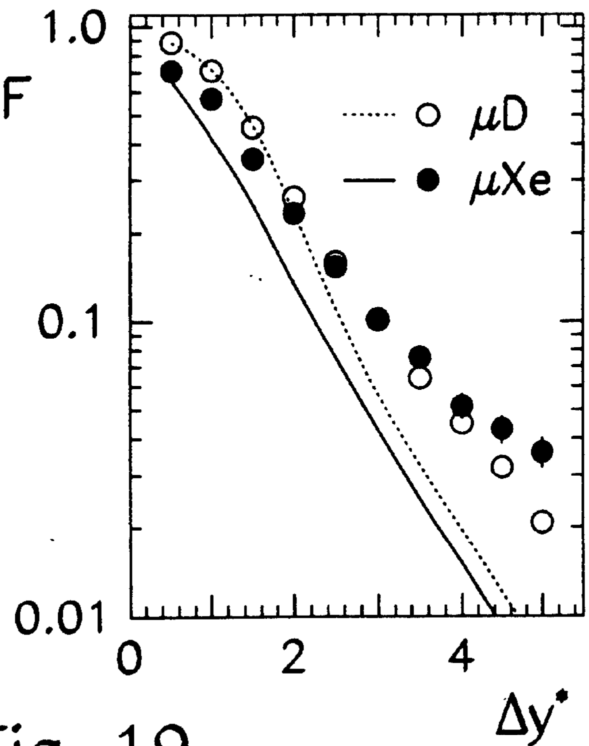

Fig. 19

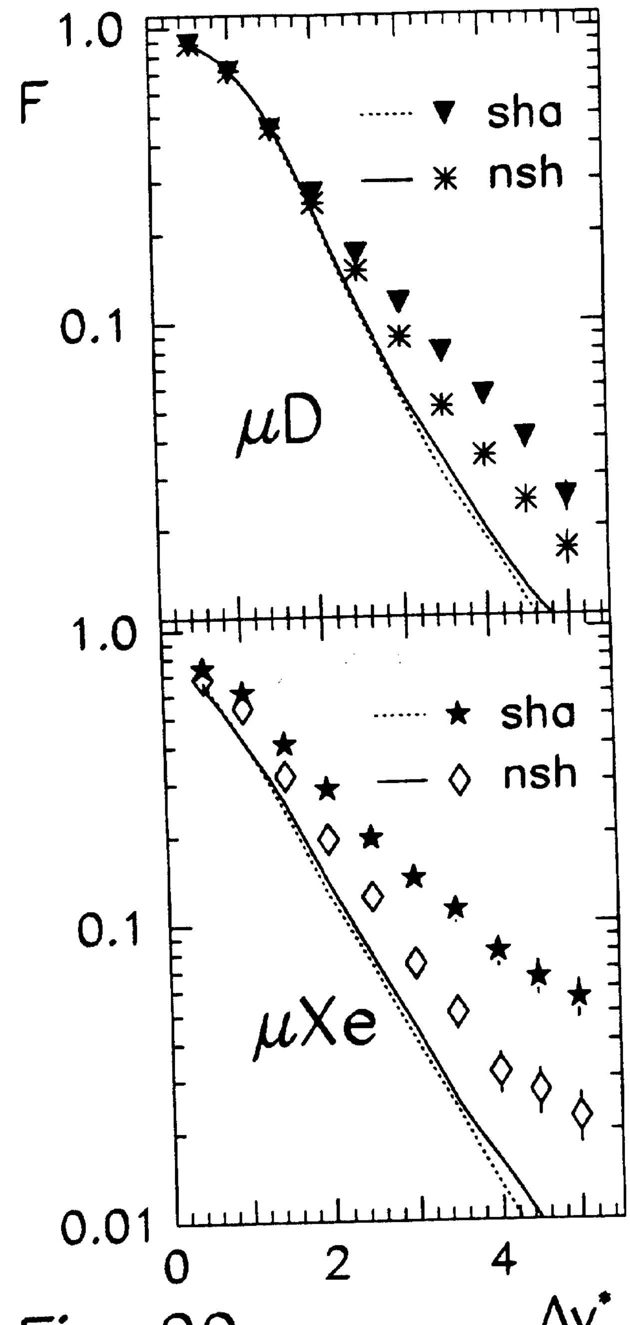

Fig. 20

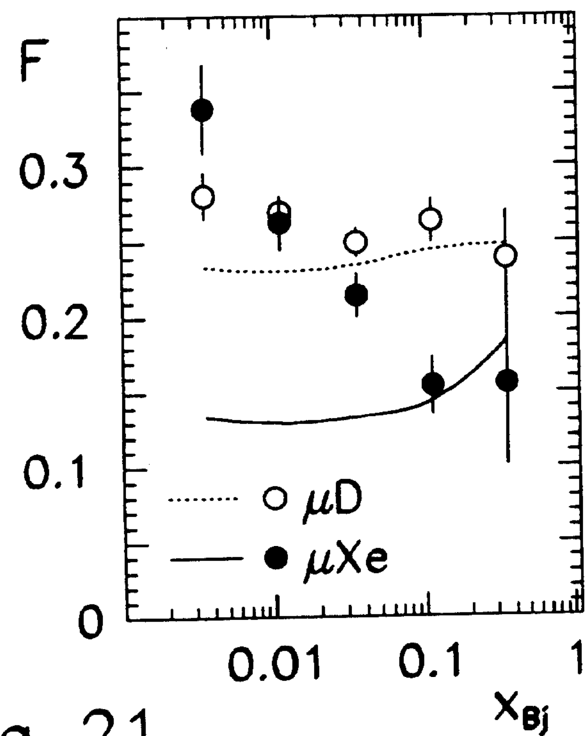

Fig. 21

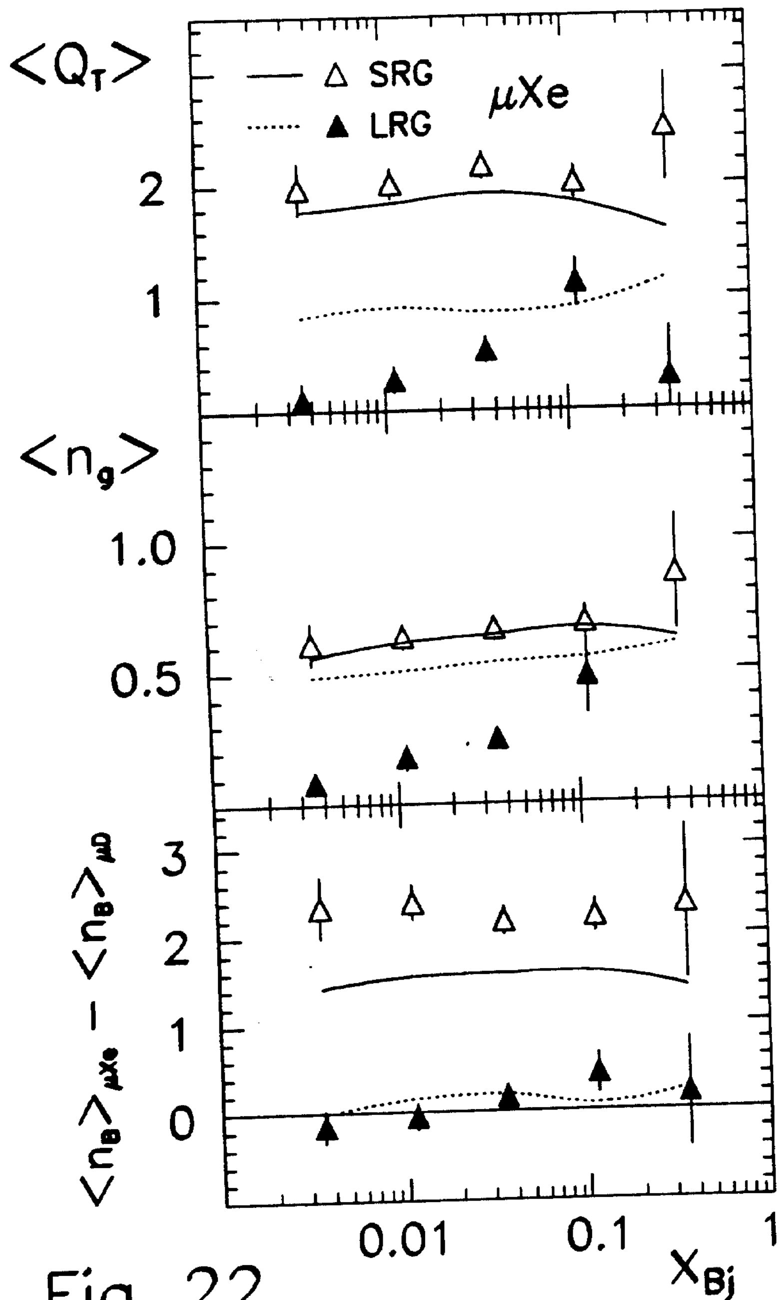

$\langle Q_T \rangle$
SRG
LRG
μXe
2
1
$\langle n_g \rangle$
1.0
0.5
$\langle n_B \rangle_{\mu Xe} - \langle n_B \rangle_{\mu D}$
3
2
1
0
0.01
0.1
1
X_{Bj}

Fig. 22

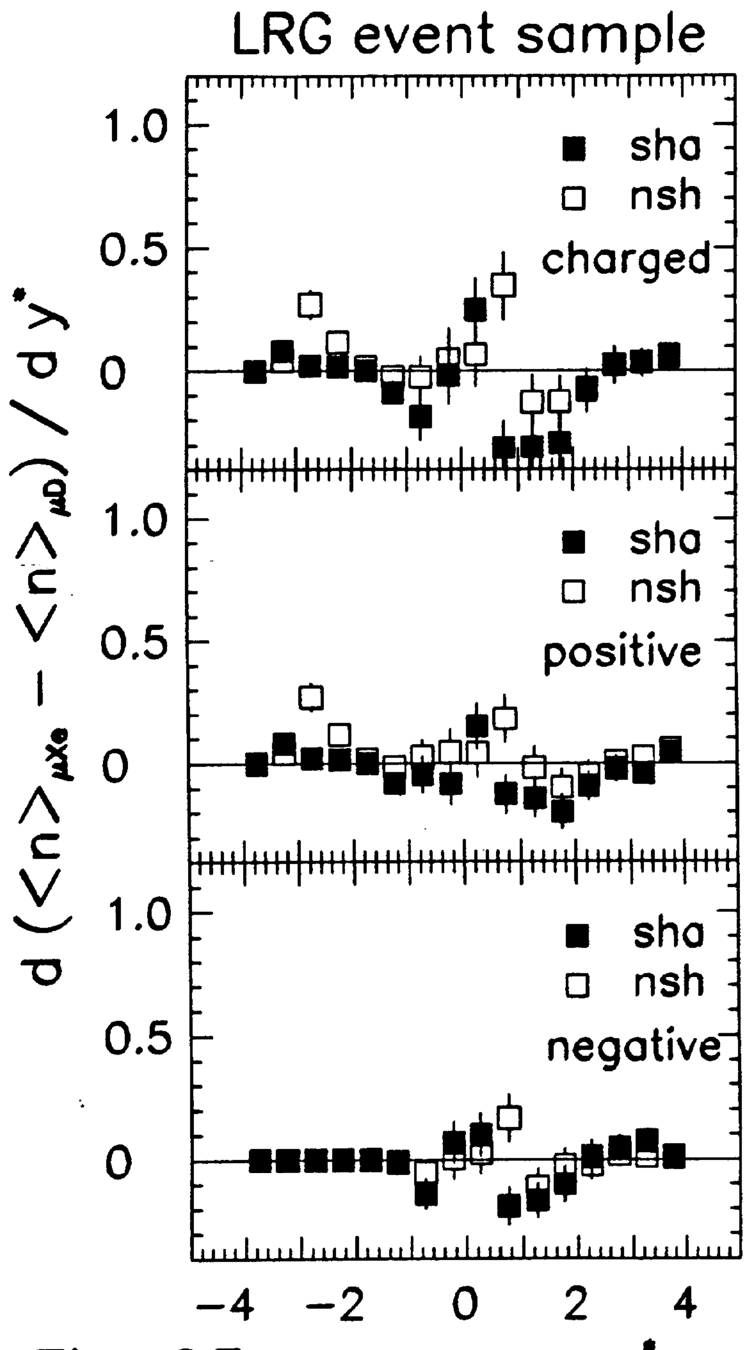
LRG event sample
sha
nsh
charged
positive
negative
1.0
0.5
0
−4
−2
0
2
4
d (<n>$_{\mu Xe}$ − <n>$_{\mu D}$) / d y*
y*

Fig. 23

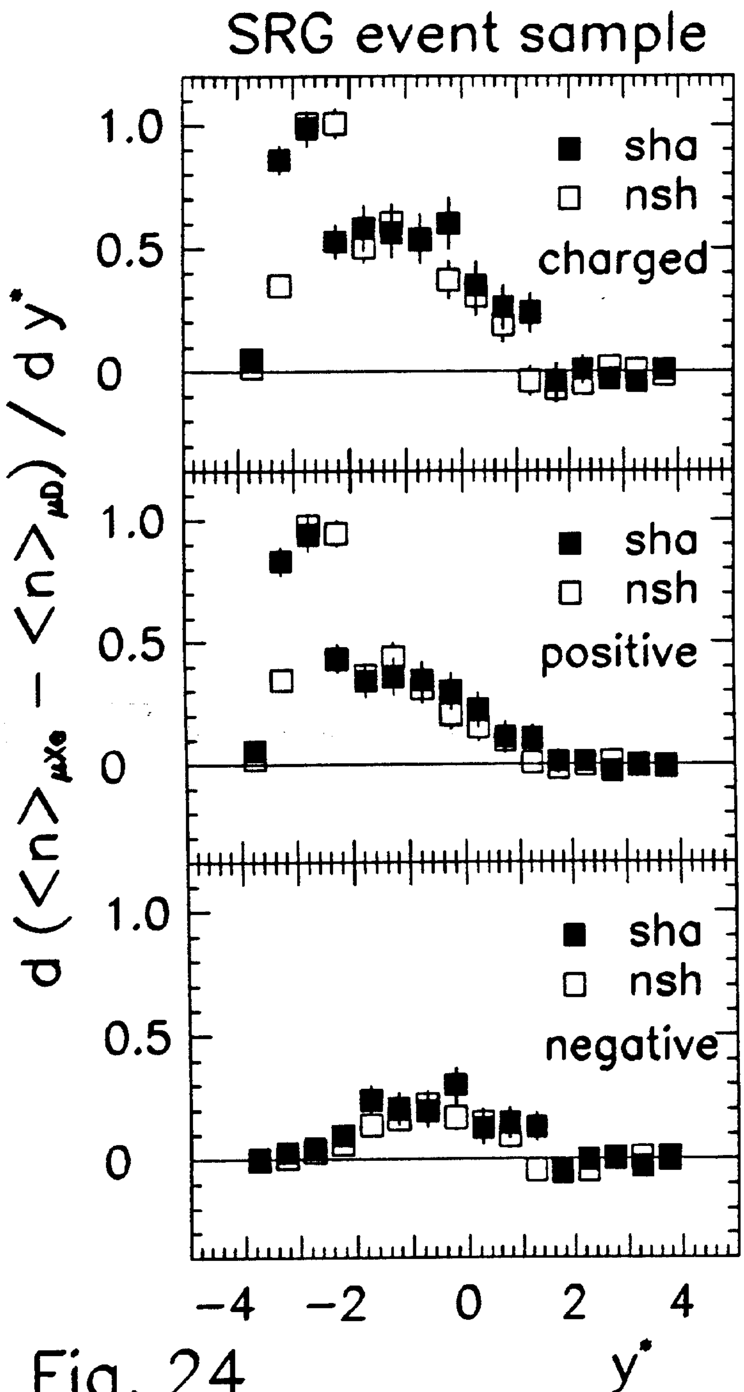
SRG event sample
sha
nsh
charged
positive
negative
1.0
0.5
0
-4
-2
0
2
4
d (<n>_μXe − <n>_μD) / d y*
y*
Fig. 24

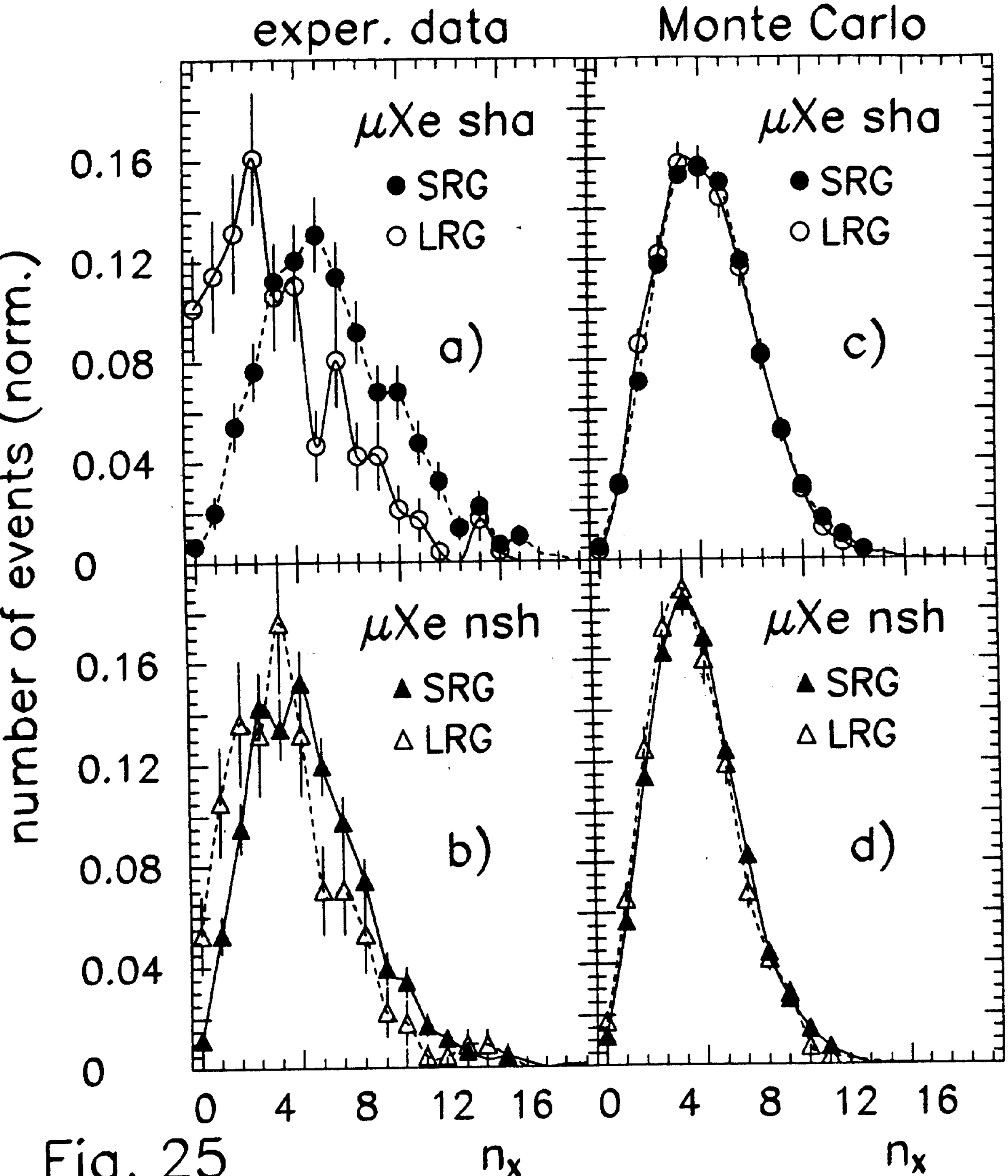
exper. data
Monte Carlo
μXe sha
● SRG
○ LRG
a)
c)
μXe nsh
▲ SRG
△ LRG
b)
d)
number of events (norm.)
0
0.04
0.08
0.12
0.16
0
4
8
12
16
n_x

Fig. 25

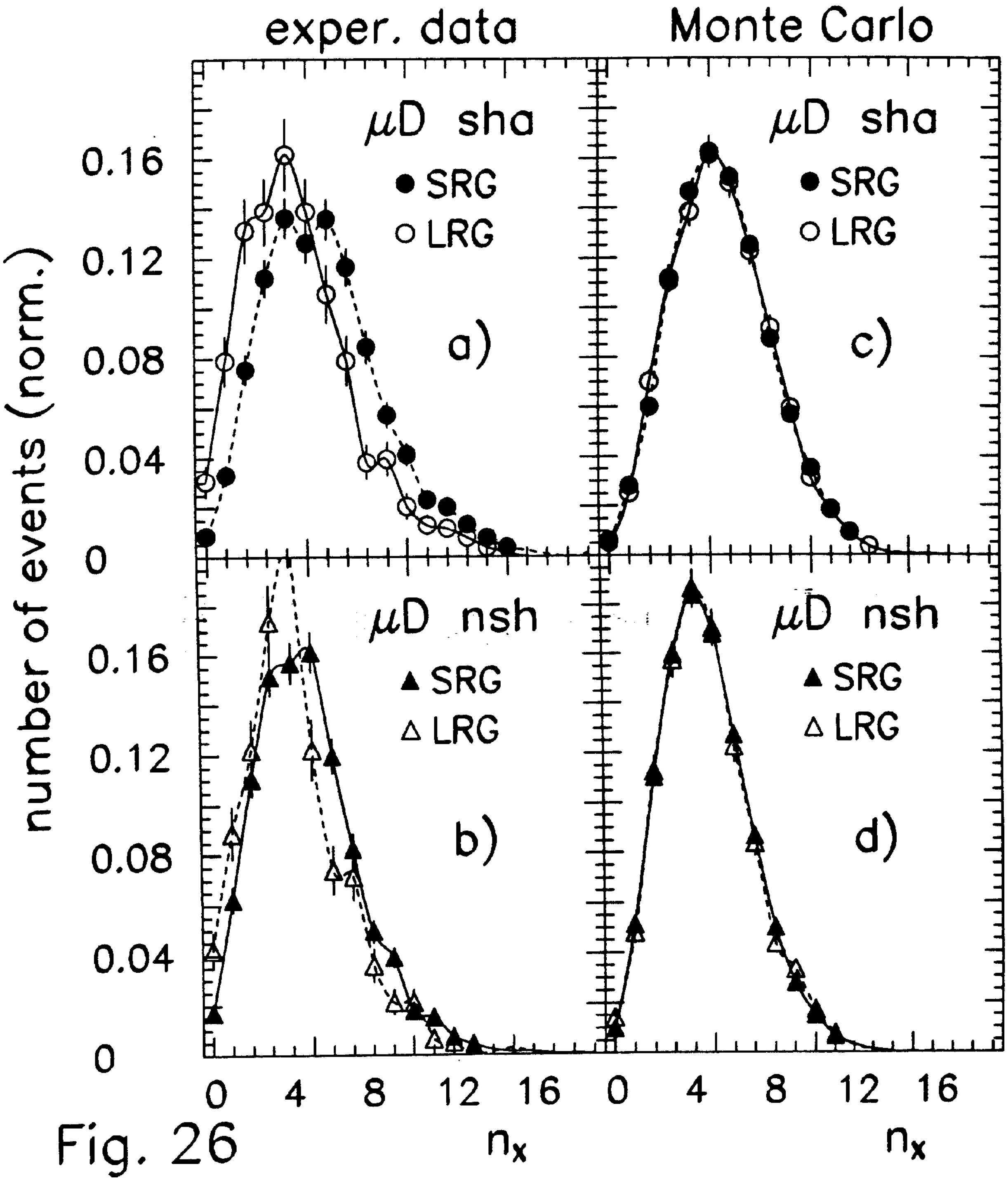
exper. data
Monte Carlo
number of events (norm.)
0.16
0.12
0.08
0.04
0
μD sha
● SRG
○ LRG
a)
c)
μD nsh
▲ SRG
△ LRG
b)
d)
0
4
8
12
16
n_x

Fig. 26

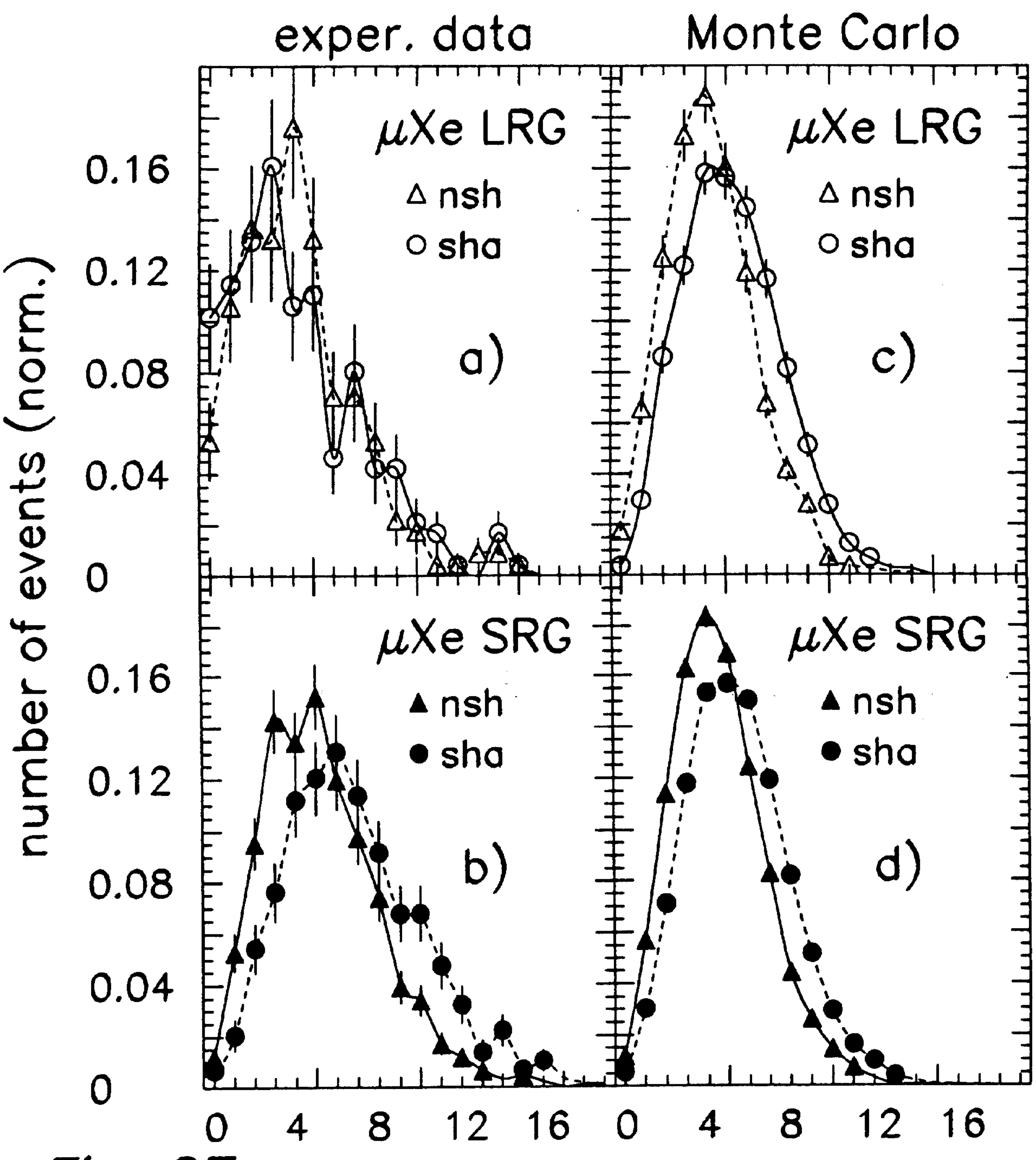
exper. data
Monte Carlo
μXe LRG
△ nsh
○ sha
a)
c)
μXe SRG
▲ nsh
● sha
b)
d)
number of events (norm.)
0
0.04
0.08
0.12
0.16
0
4
8
12
16
n_x

Fig. 27

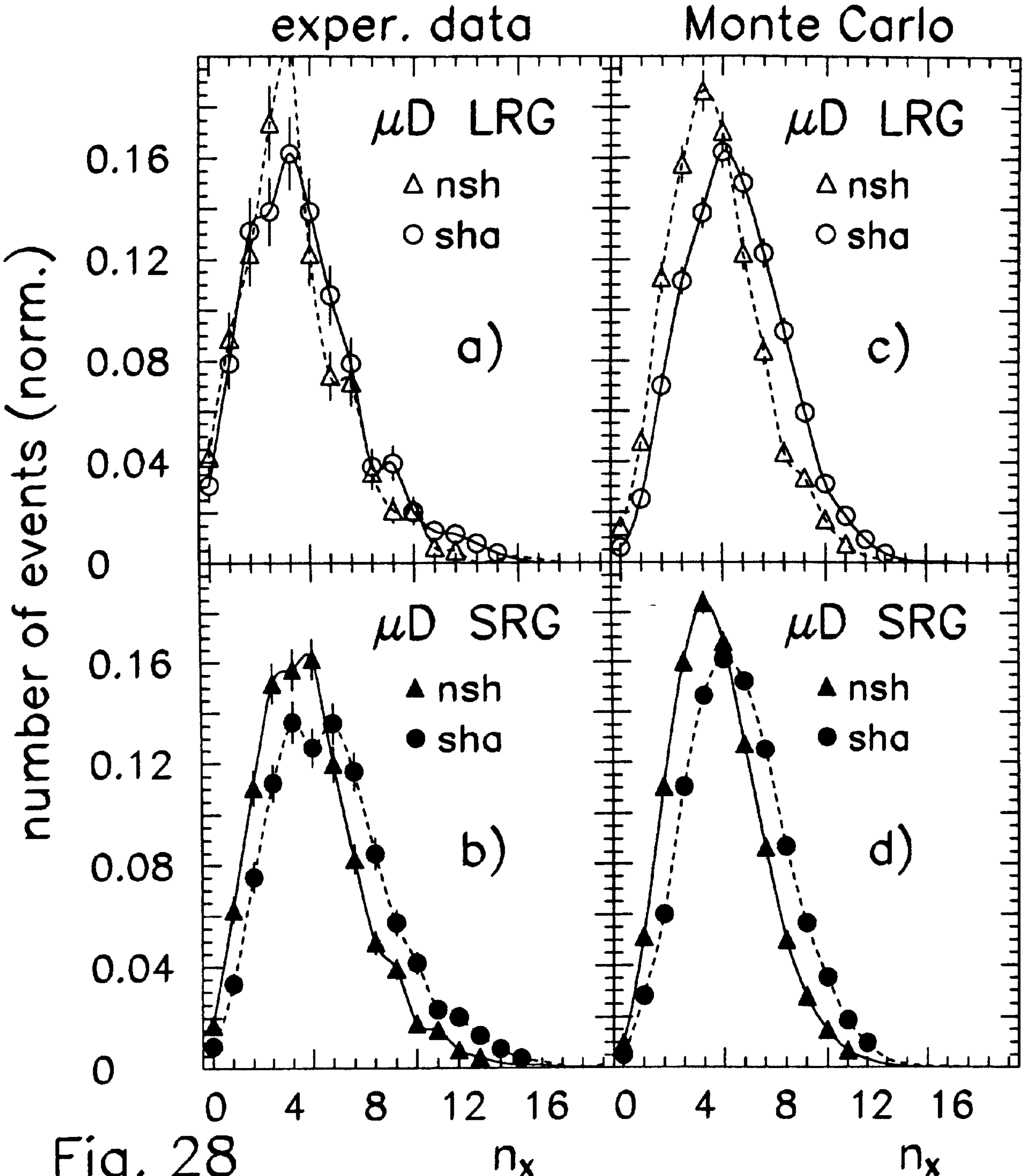
exper. data
Monte Carlo
number of events (norm.)
μD LRG
Δ nsh
○ sha
a)
c)
μD SRG
▲ nsh
● sha
b)
d)
0
0.04
0.08
0.12
0.16
0
4
8
12
16
n_x

Fig. 28